國立交通大學

電資學院光電顯示科技產業研發碩士班

碩士論文

超大橫向長晶應用於多晶矽鍺薄膜電晶體之研究

Study on Super lateral-growth Crystallization for Polycrystalline SiGe Thin Film Transistor

研 究 生：李啟銘

指導教授：劉柏村 博士

中 華 民 國 九 十 六 年 六 月

超大橫向長晶應用於多晶矽鍺薄膜電晶體之研究

Study on Super lateral-growth Crystallization for Polycrystalline SiGe Thin Film Transistor

研 究 生：李啟銘　　Student：Chi-Ming Lee

指導教授：劉柏村 博士　　Advisor：Dr. Po-Tsun Liu

國 立 交 通 大 學

電機學院光電顯示科技產業研發碩士班

碩 士 論 文

A Thesis
Submitted to College of Electrical and Computer Engineering
National Chiao Tung University
in partial Fulfillment of the Requirements
for the Degree of
Master
In

Industrial Technology R & D Master Program on
Photonics and Display Technologies

June 2007
Hsinchu, Taiwan, Republic of China

中 華 民 國 九 十 六 年 六 月

超大橫向長晶應用於多晶矽鍺薄膜電晶體之研究

研究生：李啟銘　　　　　　　指導教授：劉柏村 博士

國立交通大學

電機學院光電顯示科技產業專班

摘要

在此論文裡，我們以準分子雷射結晶法為基礎，探討超大橫向長晶對於多晶矽鍺薄膜電晶體電特性的影響。依據結晶結構以及元件通道材料兩個觀點去改善多晶矽鍺薄膜電晶體之特性。

矽原子與鍺原子具有不同的溶點以及4%差異的晶格常數。這結果會造成鍺原子的偏析和矽鍺薄膜的應力。這兩者可借由拉曼頻譜來決定晶粒中合金的組合成份以及殘留的應力。根據材料分析的結果，經過連續橫向結晶後，多晶矽鍺薄膜具有不同濃度的鍺原子分布在晶粒中，起因在於橫向結晶的期間，薄膜開始橫向長晶的位置到晶粒邊界的位置之間發生鍺原子的偏析。實驗結果，超大橫向長晶對於矽鍺薄膜應力的釋放具有很好的功效。至於結構性質也將透過原子力顯微鏡與掃描式電子顯微鏡來描述。

鍺原子的偏析會造成鍺含量高與鍺含量低兩種區域。當鍺濃度逐漸增加地分佈在電晶體的通道之中會造成通道能隙的改變。鍺含量高的區域相對於鍺含量低的區域具有較低的價電帶。假如鍺含量高的區域落於源極處，將會加速電洞的排出而改善浮體效應。因為浮體效應的改善，扭結效應也會改善。

Study on Super lateral-growth Crystallization for Polycrystalline SiGe Thin Film Transistor

Student：Chi-Ming Lee Advisor：Dr. Po-Tsun Liu

National Chiao Tung University
Department of Industrial Technology R & D Master Program on Photonics and Display Technologies

Abstract

In this thesis, based on the excimer laser crystallization technique, the influences of the super lateral-growth crystallization on the electrical characteristics of polycrystalline SiGe thin film transistors have been investigated. From the two viewpoints of crystallization structure and channel material have been proposed to improve the performance of polycrystalline SiGe TFTs.

Si and Ge atoms have different melting point and 4% difference in the lattice constants. The results to make the Ge segregation and the strain of SiGe thin film. Both the alloy composition and residual strain in the grains were determined from the Raman shift. According to the material analysis results, poly-Si1-xGex thin film can be grading the Ge content across the grain after sequential lateral solidification due to the Ge segregation occurs at film initiate later growth to the grain boundary during lateral-growth crystallization. The experimental results are in good agreement with the strain relaxation of SiGe thin film by the super lateral-growth crystallization. Structural properties were characterized by atomic force microscopy (AFM) and scanning electron microscopy (SEM).

The Ge segregation to make the Ge-rich and Ge-poor region. By grading the Ge

content across the transistor channel region, the band gap will be different. The Ge-rich region has lower valence band than Ge-poor region. If the Ge-rich region at the source, the floating body effect will be improve by accelerate the hole emission. The kink effect will be improve due to improve the floating body effect.

誌 謝

在這碩士學位的兩年研究生涯中，有太多人令我心存感激。首先，要特別感謝我的論文指導老師 劉柏村教授，感謝老師在學術研究、知識、人格養成上不斷地給予指導、教誨與提攜，讓我獲益良多，使我能順利的完成碩士學位。另外，還要感謝中山物研所 張鼎張教授，在學術研究上給我正確詳盡的指導，在此致上內心最誠摯的敬意和謝意。諸位口試委員的指導和建議，也在此謹申謝意。

在此，感謝劉柏村教授實驗室中學長們兩年來的教導，此外，特別感謝王敏全、涂峻豪及陳世青學長們在製程與實驗數據上的指導，感謝工研院陳宏哲學長、材料所鄧伊茹學姐、張志榜學長、顯示所江俊德同學及中山大學謝漢伯學弟在機台設備上給與支援，也感謝NDL裡的工程師在機台上的指教與幫忙。

在這兩年的歲月裡，有歡樂也有不如意，幸好有我的最佳伙伴-唐豪與崇維陪我一起度過，還有感謝逸哲、建文、昇翰學長們、子怡學姐、柏宇、又菁同學的關心，讓被稱為三劍客的我們才能信心一起突破難關，當然還有一德、弘根、千睿學長、秀娟、宛芳、建民、任偉、原園、亞諭、立夫同學以及誼明跟逸侑學弟，有了你們讓這兩年的生活過的更精彩。

最後，我願將這份榮耀呈獻給我深愛的父母親－ 李國村先生、 王素珍女士以及我親愛的三位姐姐。感謝多年來辛苦的教導與栽培，一直在背後默默地支持與關懷我，陪我度過了許多風雨與榮耀的時光，讓我能無後顧之憂，全力衝刺學業，終於不負所望完成學業，在此獻上我內心最深的謝意。

李啟銘 2007 年6 月

Contents

Abstract (Chinese) I

Abstract (English) II

Acknowledgements IV

Contents..V

Table Captions..VII

Figure Captions..VIII

Chapter 1 Introduction

1-1 General Background 1

1-2 Motivation 3

1-3 Thesis organization 4

Chapter 2 The Principle and Experimental Procedures

2-1 α-$Si_{1-x}Ge_x$ Thin Film Deposition..6

2-2 Excimer-Laser Crystallization (ELC) Technique..................8

2-2-1 Conventional Excimer laser crystallization...........................10

2-2-2 Sequential Lateral Solidification (SLS) Process......................12

2-3 Experimental Procedures..15

2-3-1 Sequential Lateral Solidification of α-$Si_{1-x}Ge_x$ Thin Film..........15

2-3-2 Fabrication of SLS-Procssed Poly-$Si_{1-x}Ge_x$ TFTs......... 16

Chapter 3 Results and Discussion

3-1 Material Characterization of Super lateral-growth Crystallization of Poly-$Si_{1-x}Ge_x$ Thin Films……………………25

3-1-1 Raman Spectroscopy Analysis ………………………………25

3-1-2 Scanning Electron Microscope (SEM) Analysis……………...27

3-1-3 Atomic Force Microscopy (AFM) Analysis…………………..28

3-1-4 Energy Dispersive X-ray(EDS) ………………………….……29

3-2 The Crystallization Mechanism of SLS-Procssed α-$Si_{1-x}Ge_x$ Thin Films ……………………………………………..29

3-3 Electrical Characterization of SLS-Procssed Poly-$Si_{1-x}Ge_x$ TFTs………………………………………………………30

Chapter 4 Conclusion ………………………………………………..53

References 54

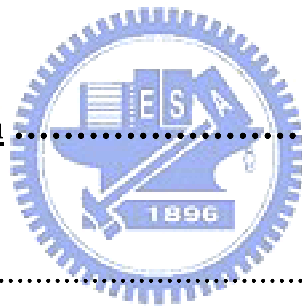

Table captions

Chapter 2

Table 2-1 Different excimer laser gases and corresponding wavelengths

Table 2-2 Detailed deposition parameters of LPCVD $Si_{1-x}Ge_x$ Thin Film

Chapter 3

Table 3-1 Raman peak position (cm^{-1})

Table 3-2 The material characteristic of the thin films laser crystallization with different laser energy

Figure Captions

Chapter 2

Figure 2-1 Band-diagram of (a) silicon and (b) germanium. Figure from [3].

Figure 2-2 Experimental data of critical thickness for SiGe layers grown at 550˚C (○) [2] and 750˚C (◇) [4] with MB equilibrium calculated line.

Figure 2-3 (a)Laser beam profile (b) conformity of overlapping and the deviation of each laser pulse.

Figure 2-4 Schematic diagrams of recrystallization mechanisms with respect to different energy density of ELA: (a) partial melting regime, (b) complete melting regime and (c) nearly complete melting (super lateral growth) regimes.

Figure 2-5 (a) Mask pattern and (b) (c) (d) schematically show the microstructural evolution that results when SLS is carried out using a narrow line beamlet.

Figure 2-6 Optical micrographs of SLS-processed film: (a)Mask patten. (b)low magnification. Straight-slit + chevron-shaped beamlet. (c) High magnification. After Secco-Etched, Straight-slit beamlet (d) chevron-shaped beamlet .The dark-field with dotted lines demarking the boundaries between the single-crystal and columnar crystal region.

Figure 2-7 The key process procedure of fabricating SLS-Procssed poly-$Si_{1-x}Ge_x$ TFTs.

Chapter 3

Figure 3-1 Raman spectra of thin films as deposited

Figure 3-2 Raman spectra of SLS-processed Si thin films irradiated with different laser energy density at room temperature

Figure 3-3 Raman spectra of SLS-processed $Si_{0.66}Ge_{0.34}$ thin films irradiated with different laser energy density at room temperature.

Figure 3-4 Raman spectra of SLS-processed $Si_{0.5}Ge_{0.5}$ thin films irradiated with different laser energy density at room temperature.

Figure 3-5 (a) The position of the Raman spectra of $Si_{0.66}Ge_{0.34}$ for 600,700,800 and 900 mJ/cm^2 (b)The line shows the position of the Si-Si mode in crystalline $Si_{0.66}Ge_{0.34}$.

Figure 3-6 (a) The position of the Raman spectra of $Si_{0.5}Ge_{0.5}$ for 600,700,800 and 900 mJ/cm^2 (b)The line shows the position of the Si-Si mode in crystalline $Si_{0.5}Ge_{0.5}$

Figure 3-7 Raman spectra of SLS-processed thin films irradiated with 600 mJ/cm^2 laser energy density at room temperature

Figure 3-8 Raman spectra of SLS-processed thin films irradiated with 700 mJ/cm^2 laser energy density at room temperature

Figure 3-9 Raman spectra of SLS-processed thin films irradiated with 800 mJ/cm^2 laser energy density at room temperature

Figure 3-10 Raman spectra of SLS-processed thin films irradiated with 900 mJ/cm^2 laser energy density at room temperature

Figure 3-11 α-Si Laser Crystallization after Secco etching

Figure 3-12 α- $Si_{0.66}Ge_{0.34}$ Laser Crystallization after Secco etching

Figure 3-13 α- $Si_{0.5}Ge_{0.5}$ Laser Crystallization after Secco etching

Figure 3-14 The proposed crystallization Mechanism for side region

Figure 3-15 The proposed crystallization Mechanism for middle region

Figure 3-16 The proposed crystallization Mechanism for grain boundary

Figure 3-17 AFM micrographs of section analysis for poly-Si films irradiated by laser energy 800 mJ/cm^2

Figure 3-18 AFM micrographs of section analysis for poly-$Si_{0.66}Ge_{0.34}$ films irradiated by laser energy 800 mJ/cm^2

Figure 3-19 AFM micrographs of section analysis for poly-$Si_{0.5}Ge_{0.5}$ films irradiated by laser energy 800 mJ/cm^2

Figure 3-20 SEM micrographs and EDX analysis results of the (a) poly-$Si_{0.66}Ge_{0.34}$ thin film.(b) poly-$Si_{0.5}Ge_{0.5}$ thin film. E = 800mJ/cm^2

Figure 3-21 EDX analysis results of the poly-$Si_{0.66}Ge_{0.34}$ thin film with different laser energy

Figure 3-22 EDX analysis results of the poly-SiGe thin film with 800 mJ/cm^2

Figure 3-23 By grading the Ge content across the grain, the band gap will be different

Figure 3-24 The proposed crystallization model for poly-Si1-xGex films crystallized by SLS-processing

Figure 3-25 shows the I_d-V_g characteristic of poly-Si and poly-$Si_{0.66}Ge_{0.34}$ devices

Figure 3-26 shows the I_d-V_d characteristic of poly-Si and

poly-$Si_{0.66}Ge_{0.34}$ devices
Figure 3-27 The proposed mechanism to improve floating body effect

Chapter 1

Introduction

1-1 General Background

In the recent years, Low-temperature polycrystalline silicon (LTPS) thin-film transistors have been widely studied because of their potential applications in high-performance displays, such as active matrix liquid crystal displays (AMLCDs) [1.1] [1.2] and active matrix organic light emitting displays (AMOLEDs) [1.3]. High-performance thin-film transistor (TFT) devices fabricated using large-grained polycrystalline Si film for the active region are desirable, as they can enable integration of various driver components directly onto the substrate in order to reduce manufacturing costs, and to increase the functionality of large-area microelectronics[1.4].

Since the device driving capability will crucially influence the performance of the integrated circuits, the mobility of the device becomes a significant problem. The mobility would be limited to a saturation value due to other unfavorable effects, such as large surface roughness [1.5] [1.6], restricted grain size, and poor low-temperature gate dielectric quality. In order to make a process viable for use in manufacturing, the material quality must be optimized for performance, throughput, and uniformity. An excimer-laser-based crystallization technique that enables controlled periodic placement of high-angle grain boundaries has been developed in order to address the problems associated with the presence of defects within the material [1.7],[1.8],[1.9]. This crystallization scheme—sequential lateral solidification (SLS)—allows one to manipulate the resulting microstructure of the polycrystalline Si film to yield a wide range of material quality: from large

defect-free single-crystal islands to uniform large-grained polycrystalline material [1.10]–[1.12].

Even though the mobility of SLS-processed poly-Si TFT can meet the requirements for many circuit applications, further enhancement of mobility is necessary for high-level system integration. Essentially, Ge incorporated in Si (i.e. $Si_{1-x}Ge_x$) can not only lower the process thermal budget, but also promote the carrier mobility; hence, $Si_{1-x}Ge_x$ seems to be a potential material for the active layer of a TFT [1.13] – [1.15].

For high speed device application, the SiGe HBT technology has made tremendous improvement in RF performance including transistor speed, gain and noise figure. The heterojunction discontinuity between the base and the emitter region resulting from the reduced bandgap of the $Si_{1-x}Ge_x$ base region suppresses the hole injection into the emitter region. The current grain of the HBT would increase due to the reduction of hole injection.

For gate engineering, the poly-Si gate electrode can be adjusted with different Ge atomic concentration to reduce resistance. This makes it become possible to replace the poly-Si gate electrode with poly-$Si_{1-x}Ge_x$ in CMOS technology.

On the other hand, for source/drain engineering, $Si_{1-x}Ge_x$ could also be adopted as a diffusion-source for the formation of shallow junction. poly-$Si_{1-x}Ge_x$ has the advantage of not only reducing the sheet resistance of the S/D regions but also lowering the temperature for dopant activation. It is clear that a significant reduction in S/D resistance was indeed obtained by using a thicker poly-SiGe film.

For channel engineering, High performance $Si_{1-x}Ge_x$ channel CMOS on (100) and (110) Si surfaces with process-induced strained-Si technologies was

fabricated and compared to Si channel devices. The mechanism of stress-induced performance enhancements was systematically investigated. It has been demonstrated that MOSFETs with strained $Si_{1-x}Ge_x$ channel layer exhibited enhanced carrier mobility and superior device performance.

1-2 Motivation

Recently, many compound materials have been adopted as the channel material to improve the device properties [1.16] [1.17]. Among them, the polycrystalline silicon-germanium (poly-$Si_{1-x}Ge_x$) thin film seems to be an excellent candidate for the channel active layer because of the high carrier mobility of Ge atom [1.18] [1.19]. Poly-$Si_{1-x}Ge_x$ thin film has been widely used in nowadays high-performance semiconductor devices.

Nowadays, low-temperature poly-Si films are successfully realized with two different techniques, i.e., the excimer laser annealing [1.20] [1.21] and metal-induced solid phase crystallization of a-Si thin films [1.22]. According to the results reported by Julie A. Tsai *et al.*, poly- $Si_{1-x}Ge_x$ TFTs have been found to have higher mobility than similarly processed poly-Si TFTs .

However, most of the poly-$Si_{1-x}Ge_x$ TFTs were fabricated by using conventional solid-phase crystallization [1.23]. No studies have been conducted for the SLS-processed poly-$Si_{1-x}Ge_x$ TFT.

In this paper, we studied material characterization of SLS-procssed poly-$Si_{1-x}Ge_x$ thin films and electrical characterization of SLS-procssed poly-$Si_{1-x}Ge_x$ TFTs.

1-3 Thesis organization

Chapter 1 Introduction

1-1 General Background

1-2 Motivation

1-3 Thesis Organization

Chapter 2 The Principle and Experimental Procedures

2-1 α- $Si_{1-x}Ge_x$ Thin Film Deposition

2-2 Excimer-Laser Crystallization (ELC) Technique

2-2-1 Conventional Excimer laser crystallization

2-2-2 Sequential Lateral Solidification (SLS) Process

2-3 Experimental Procedures

2-3-1 Sequential Lateral Solidification of α-$Si_{1-x}Ge_x$ Thin Film

2-3-2 Fabrication of Super lateral-growth Crystallization of Poly-$Si_{1-x}Ge_x$ TFTs

Chapter 3 Results and Discussion

3-1 Material Characterization of Super lateral-growth Crystallization of Poly-$Si_{1-x}Ge_x$ Thin Films

3-1-1 Raman Spectroscopy Analysis

3-1-2 Scanning Electron Microscope (SEM) Analysis

3-1-3 Atomic Force Microscopy (AFM) Analysis

3-1-4 Energy Dispersive X-ray(EDS) Analysis

3-2 The Mechanism of Super lateral-growth Crystallization of α-$Si_{1-x}Ge_x$ Thin Films

3-3 Electrical Characterization of Super lateral-growth Crystallization of poly- $Si_{1-x}Ge_x$ TFTs

Chapter 4 Conclusion

References

Chapter 2

The Principle and Experimental Procedures

2-1 α-$Si_{1-x}Ge_x$ Thin Film Deposition

Both silicon and germanium are elements of group IV and they have diamond structure with band-gap energies of 1.12 eV and 0.66 eV at 300K, respectively [Figure 2-1]. The valence-band of silicon has maximum at Γ-point and it consists of light hole (lh), heavy hole (hh) and spin-orbit (so) hole bands. The lh and hh are degenerate at Γ-point while the so has 44 meV split from the others bands. The conduction-band minima is located near X along Γ-X direction (denoted Δ) and it is six-fold degenerate. Germanium has a valence-band structure similar to silicon but spin-orbit split is larger (290 meV). On the other hand, the conduction-band minimum is located at L-point and consists of eight degenerate states. Similar structural and chemical properties of these materials allow a binary alloy of $Si_{1-x}Ge_x$ that is continuously variable from pure silicon ($x=0$) to pure germanium ($x=1$). The band-structure of $Si_{1-x}Ge_x$ is silicon-like for $0 \leq x < 0.85$ and germanium-like for $0.85 < x \leq 1$ [2.1]. Though, the band-gap energy is a non-linear relation depending strongly on germanium amount and temperature [2.2] [2.3]. Empirical result of the band-gap reduction (ΔE_g) for a strained $Si_{1-x}Ge_x$ layer grown on silicon substrates with the germanium content in a technologically interesting range [2.4] [2.5] is given by the following relation

$$\Delta E_g = E_g(Si) - E_g(Si_{1-x}Ge_x) = 0.896x - 0.396x^2, \qquad \textit{for } x \leq 0.3 \quad \text{(Eq. 2.1)}$$

Although desirable, it is not possible to grow thick strained layers with much higher germanium content than 30% in a device structure due the lattice

mismatch between silicon and germanium. The lattice constant $a(Si_{1-x}Ge_x)$ for unstrained $Si_{1-x}Ge_x$ is given by the following empirical relation [2.6]:

$$a(Si_{1-x}Ge_x) = a(Si)(1-x) + a(Ge)x - 0.02393x + 0.01957x^2 + 0.00436x^3,$$

for all x(Eq. 2.2)

This makes it difficult to deposit thick $Si_{1-x}Ge_x$ layers with high germanium content without introducing defects into the material due to high induced strain in the lattice [2.7]. The strain in $Si_{1-x}Ge_x$ layers is released by formation of dislocations above a certain critical thickness (h_C) [2.8]. This thickness is also growth temperature dependent and h_C becomes thinner for high growth temperature. A practical growth temperature range for $Si_{1-x}Ge_x$ layers is 550-750 ˚C.

In the literature, Matthews and Blackeslee (MB) model [2.8] is one of the earliest theories about strain relaxation of SiGe layers and it shows a diagram of critical thickness versus germanium amount. MB model calculates critical thickness values, $h_{C,eq}$ for $Si_{1-x}Ge_x$ layers based on the equilibrium between two competing forces; the force exerted by the misfit strain and the tension in the dislocation line. Later it was demonstrated that MB equilibrium model predictions were not consistent with the experimental data of critical thickness and $Si_{1-x}Ge_x$ layers with thickness above $h_{C,eq}$ could be grown. The reason for the failure of MB model is that it is too simple and it has not considered nucleation, propagation, and interaction of dislocations. Figure 2-2 shows the experimental data for h_C and $h_{C,eq}$ for different Ge amounts. $Si_{1-x}Ge_x$ layers with thickness above $h_{C,eq}$ line are called meta-stable and strain relaxation occurs by post-annealing treatment. More accurate theories were proposed afterwards to estimate h_C for SiGe layers based on non-equilibrium approach [2.9].

Recent reports have shown that the critical thickness diagram in Figure 2-2 cannot be applied directly for SiGe layers grown on the patterned substrates. Thicker strained layers can be grown selectively1 whereas the meta-stable region shrinks for $Si_{1-x}Ge_x$ layers grown non-selectively [2.10 - 2.12]. The discrepancy of the experimental data in the later case is due to injection of defects from the polycrystalline layer into the epitaxial part. The increase in h_C for the selectively grown $Si_{1-x}Ge_x$ layers is due to strain distribution of these layers leading to a more strain relaxation closer to the edge of the oxide [2.13].

The other results about the strain relaxation of thin $Si_{1-x}Ge_x$ layers demonstrate that the strain relaxation does not occur though formation of misfit dislocations but through creation of surface roughening [2.14 - 2.16].

In recent, low temperature poly-$Si_{1-x}Ge_x$ thin film transistors (LTPSG TFTs) also have been studied due to the lower process temperature of $Si_{1-x}Ge_x$ in comparison with Si. Indeed, the lower melting temperature of Ge (1211 K) compared with Si (1683 K) means that poly-$Si_{1-x}Ge_x$ alloys have lower processing temperature. Several key fabrication processes, such as thin film deposition , thin film crystallization, and dopant activation can be carried out at lower temperature. In this work, we investigate the formation of poly- $Si_{1-x}Ge_x$ films by using a XeCl pulsed excimer laser to induce either alloying (PLIA) or crystallization (PLIC) processes.

2-2 Excimer-Laser Crystallization (ELC) Technique

Among all of the current recrystallization methods of a-Si, excimer laser is the most promising solution for future high-performance poly-Si TFTs on glass

and thus attracts much attention. The novel treatment technology, ELA, was introduced for low temperature recrystallization of SiGe films in this investigation. Excimer laser is the most effective and powerful UV light source, and that has been widely applied on the semiconductor industry, such as lithography, thin film fabrication and post annealing. Various gas is filled in a laser resonant chamber and would irradiate strong UV light under a transient high voltage discharge. Depending on the laser gas, different wavelength can be obtained ranging from 157-351 nm, as shown in Table 2-1

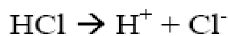

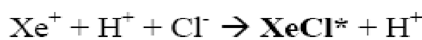

In conventional technologies, amorphous silicon films can be furnace annealed as high as 600°C above for a long period, reaching the solid phase crystallization. Besides, rapid thermal annealing (RTA) is also widely applied on thin film treatment, but it will induce large thermal stress in silicon films. ELA behaves direct energy processing that the surface can be heated by laser beam. ELA technology, strictly speaking, is not a real low temperature process, higher than 700°C in the top of laser absorption region, but this high-temperature absorption region is very shallow, 20-nm only, and the sustained time is as short as 10~100 nanoseconds. Since the α-Si has strong absorption for UV light (absorption coefficient > $10^6 cm^{-1}$) , the energy can be transferred to the Si surface effectively and cause silicon to melt. Liquid-phase crystallization methods, which have been used in low-temperature poly-Si technology, have also been adopted in the field of recrystallization of α-$Si_{1-x}Ge_x$ thin film.

2-2-1 Conventional Excimer laser crystallization

However, the laser pulse duration, typically 10~100 nanoseconds, is quite short so that the melted Si solidifies in a few hundred nanoseconds, leaving the glass or even plastic substrate undamaged from the heat. The prime disadvantages of ELA for poly-Si recrystallization lie in the process uniformity and its small process window. Because the beam width of pulsed excimer laser is only a few millimeters or less, a continuous scan with overlapping of laser beam is required to recrystallize α-Si in a large area. Consequently, the accuracy of overlapping and also the deviation of each laser pulse affect the given energy as well as crystalline uniformity after ELA, as show in Figure 2-3.

Moreover, amorphous or crystalline in terms of two major transformation regimes (low and high energy density) and one minor transformation regime (SLG)[2.17]. There are three recrystallization mechanisms corresponding to different laser energy: partial melting, complete melting and nearly complete melting (super lateral growth) regimes, as show in Figure 2-4.

Both partial melting and complete melting contribute to small grain size; only a narrow laser energy window can result in nearly complete melting regime where the unmelted islands act as solidification seeds from which a lateral grain growth commences.

1. Low energy density (partial melting) regime:

In the partial melting regime, the energy density of incident laser pulse is above the surface melting threshold but below the complete melt-through energy density (i.e., melting depth < film thickness). The α-Si thin film can be partially melted and subsequently can be crystallized. Explosive crystallization of α-Si thin film occurs at the beginning of the transformation and follows by

vertical regrowth. The early trigger of explosive crystallization may be attributed either to the presence of microcrystalline clusters and/or to the possible presence of impurities such as hydrogen. In this regime, there is an increase in the grain size with increases in the laser energy density. This occurs up to the point at which the average grain radius is approximately equal to the film thickness.

2. High energy density (complete melting) regime :

In the complete melting regime, the energy density of incident laser pulse is enough high to lead to a complete melting of the α-Si thin film and no unmelted Si remains. A sudden increase in the melt duration, which is observed at the transition from the low to high energy density regime, is strong significant of the transition from partial melting and regrowth to complete melting. The complete-melting Si thin film is then followed by significant supercooling of the liquid before the occurrence of the transformation to the solid phase. In this regime, the final microstructure is insensitive to large variations in laser energy densities. For low substrate temperature, fine-grained and small-grained poly-Si thin films are observed. In addition, amorphization of the poly-Si thin film is found for thinner film thickness.

3. SLG regime

In the near complete melting regime, the energy density of the incident laser pulse leads to a unmelted α-Si thin film composed of discrete islands (i.e. melting depth ≈ film thickness). At this point, with a small increase in the energy density, an extremely sharp increase in the grain size occurs. Due to the technological significance of large-grained poly-Si thin film and its dramatic nature, this regime is also referred as the super lateral growth (SLG) regime. With further slight increases in laser energy density, a dramatic reversal in the

microstructural trend is observed in that fine-grained poly-Si thin film is obtained. This transition marks the end of the low energy density regime and the beginning of the high energy density regime.

In view of the above interpretations imposed on the low and high energy density regimes, it can be argued that the large-grained poly-Si thin film obtained in the SLG regime is a consequence of the liquid phase regrowth from the discontinuous and small solid seeds, which are never fully melted.

In other word, the SLG regime corresponds to the condition at which point near-complete melting of the film occurs to the extent that the unmelted a-Si thin film no longer forms a continuous layer; instead, the residual Si is composed of discrete island. Hence, as the temperature begins to drop, growth from these clusters can proceed. Depending on the separation distance between these seeds, it is possible for significant lateral growth to take place before the impingement of the grain occurs. However, there is a limit to the maximum lateral growth distance, which can be achieved as continuous cooling of the liquid layer via conduction to the substrate eventually would lead to copious nucleation of solids in bulk liquid ahead of the interface. High substrate temperature lead to lower quenching rates, which in turn provides more time for lateral growth to take place before bulk nucleation intervenes. In addition, the SLG distance will also increase with increasing film thickness, decreasing thermal conductive of the substrate, and increasing the laser pulse duration [2.18].

2-2-2 Sequential Lateral Solidification (SLS) Process

The maximum length of the C-SLG-grown grains that can be attained

using a singlepulse irradiation will be limited by nucleation to a few micrometers. As such, there will always be an associated degree of limitations in controlling the resulting microstructure.

For those C-SLG approaches that utilize shaping of the incident beam, however, a potent option exists for trivially overcoming the above limitation inherent with singlepulse irradiation; by simply and appropriately repositioning the relative position of the sample with respect to the incident beam between pulses, it is possible to induce further lateral growth of the previously formed grains via epitaxial growth by seeding from the grains.

This particular process of iteratively inducing C-SLG in a coordinated manner is referred to as sequential lateral solidification (SLS), and it represents an effective and efficient means to manipulate the microstructure of a thin Si film[2.19 - 2.22].

The nature of the SLS process dictates that, in addition to the basic C-SLG requirement of inducing complete melting in controlled locations, the following conditions areto be satisfied : 1. the relative translation be in the direction of the lateral growth and 2. the per-pulse translation distance be less than the C-SLG distance. Satisfying these additional conditions ensures that the subsequent irradiation leads to continuous epitaxial lateral growth of the grains. (Less systematic SLS approaches that do not entirely satisfy the above requirements, and that lead to large-grained materials, are still possible, however.) Figure 2-5 show the microstructure that results when the molten zone is narrow, and lateral growth is terminated by the two opposing growth fronts colliding at the center. When the molten zone is sufficiently wide, bulk nucleation of solids inevitably occurs in the middle of the completely molten region.

The illustrated microstructure corresponds to that which is obtained in a directionally solidified material, and it simply reflects the tendency of the grain boundaries (as well as dislocations and sub-boundaries) to orient themselves approximately perpendicular to the advancing solid-liquid interface [2.23].

This particular correlation between the solidified microstructure and the solidifying interface can be systematically exploited by engineering the shape of the irradiated region to create a variety of low-defect-density crystalline Si films. The principle can also be used to create large-grained and uniform polycrystalline Si films, or a directionally solidified microstructure with perfectly parallel grain boundaries.

Multiple beamlets were formed using projection irradiation of an excimer laser beam, where a patterned UV mask with chevron shaped apertures was used to shape the original excimer laser beam into multiple beamlets, as shown in Figure 2-6. This ability to simultaneously process multiple regions over a large area makes the SLS process efficient, while the fact that the process requirements (i.e., inducing complete melting mainly in the irradiated portion of the film and precise microtranslation of the sample with respect to the incident beamlets) can be easily satisfied, makes the process effective. (Preliminary results show that the energy density processing window can range from approximately 20% for 500 Å thick Si films to over 40% for 2200 Å thick Si films.) It is important to note that the size of the single-crystal region is determined by varying the overall width of the beamlet and the total translation distance, and the number and location of these regions can be precisely controlled by using an appropriately patterned mask.

The SLS method is a flexible approach that can be 1. implemented using various combinations of pulsed energy sources and beam-delivery schemes, 2.

executed using various beam/beamlet patterns and translation sequences, and 3.applied to materials other than Si, including non-elemental semiconductors such as Si-based IV-IV alloys.

2-3 Experimental Procedures

2-3-1 Sequential Lateral Solidification of α-$Si_{1-x}Ge_x$ Thin Film

In order to prepare the sample for α-$Si_{1-x}Ge_x$ thin film deposition, silicon dioxide (SiO_2) with a thickness of 2 μm was thermally growth on bare silicon wafers by furnace. These oxidized silicon wafers were used as the starting substrate in order to imitate the real glass substrate. Before deposition of α-$Si_{1-x}Ge_x$ thin film, a smooth initial Si layer with a thickness of 50Å to improve the nucleation of $Si_{1-x}Ge_x$ on SiO_2. This kills the long incubation time found for α-$Si_{1-x}Ge_x$ thin film deposition on an oxide surface [2.24]. And then, $Si_{1-x}Ge_x$ thin films with a thickness of 450Å were deposited on the oxidized Si wafers by low-pressure chemical vapor deposition (LPCVD). The Ge atomic concentration in the as-deposited $Si_{1-x}Ge_x$ thin film was adjusted by varying the germane (GeH_4) to silane (SiH_4) gas flow ratio. Detailed deposition parameters were listed in the Table 2-2.

The substrates were cleaned employing a standard RCA-process before loading them into the deposition tube. The pulsed-XeCl (308nm) sequential lateral solidification of α-$Si_{1-x}Ge_x$ thin film was carried out in 760 Torr at room temperature. The crystallization apparatus consisted of an excimer laser operating at 308 nm (XeCl) and with an UV projection system, a patterned mask, and a submicrometer-precision translation stage. The pattern consisted

of an array of narrow parallel slits such that only the portion of the original beam that passed through the slits was transmitted. For the results reported in this letter, the relative positions of the mask, imaging lens, and sample were adjusted to yield a pattern demagnification ratio of approximately 5X. At this demagnification, the image of each slit had a width of 5 μm at the sample plane.

Several material analysis techniques were used to investigate the relation between the morphology of crystallized poly-Si thin films and laser process conditions. Scanning electron microscopy (SEM) was utilized to analyze the grain structure and grain size. In order to facilitate the SEM observation, the samples were processed by Secco-etch before analysis. Secco-etch preferably etches the grain boundary in poly-$Si_{1-x}Ge_x$ thin film. The atomic bonding changes and the crystallinity of as-deposited $Si_{1-x}Ge_x$ film induced by the laser annealing were studied by Raman spectroscopy.

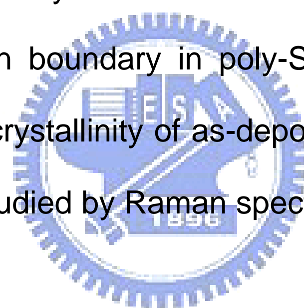

2-3-2 Fabrication of SLS-Procssed Poly-$Si_{1-x}Ge_x$ TFTs

The procedure of fabricating top-gate, self-aligned n-channel poly-$Si_{1-x}Ge_x$ TFTs with sequential lateral solidification is illustrated in Figure 2-7. α-$Si_{1-x}Ge_x$ thin film with a 450Å thickness was first deposited on oxidized silicon substrate by low pressure chemical vapor deposition (LPCVD) at 450°C using SiH_4 and GeH_4 as gas precursors. The GeH_4 to SiH_4 gas flow ratio was adjusted to obtain α-$Si_{1-x}Ge_x$ thin films with different Ge atomic concentration. Before deposition of α-$Si_{1-x}Ge_x$ thin film, a smooth initial Si layer with a thickness of 50Å was deposited by LPCVD to improve the nucleation of α-$Si_{1-x}Ge_x$ on SiO_2. This killed the long incubation time found for α-$Si_{1-x}Ge_x$ thin film deposition on

an oxide surface. After clean process, the wafer was then subjected to 308nm XeCl excimer laser annealing.

After laser irradiation, poly-$Si_{1-x}Ge_x$ thin film was defined into individual active island. Next, 1000Å TEOS gate oxide was deposited by low pressure chemical vapor deposition (LPCVD) at 700°C. A 3000Å poly-Si film was then deposited by low pressure chemical vapor deposition (LPCVD). The poly-Si was etched by TEL oxide etcher form poly-gate electrodes. After the poly-gate electrodes were patterned, a self-aligned P^+ ion implantation with the dose concentration of

1×10^{15} cm^{-2} was carried out to form the source and drain regions. Then, LPCVD annealing was performed to activate the implanted dopants and recrystallize the source and drain region at 600°C for 40 min. A 5000Å TEOS oxide was deposited by HDPCVD at 350°C as passivation layers. After contact holes opening, Al was deposited by thermal evaporation and patterned to form the electrical connecting pads.

The typical transfer and output characteristics of the SLS-Procssed poly-$Si_{1-x}Ge_x$ TFTs were measured by HP4156 precise semiconductor parameter analyzer. The device parameters including field-effect mobility, threshold voltage, subthreshold swing and on/off current ratio were extracted from the measured characteristics. The electrical performances of the SLS-Procssed poly-Si controlling samples were also estimated to compare with the SLS-Procssed poly- $Si_{1-x}Ge_x$ counterparts.

Table 2-1 Different excimer laser gases and corresponding wavelengths

Laser Gas	XeF	XeCl	KrF	KrCl	ArF	F_2
λ(nm)	351	308	248	222	193	157

Table 2-2 Detailed deposition parameters of LPCVD $Si_{1-x}Ge_x$ Thin Film.

Temperature (°C)	Pressure (mTorr)	SiH_4 (sccm)	GeH_4 (sccm)
450	300	60	0 4 8

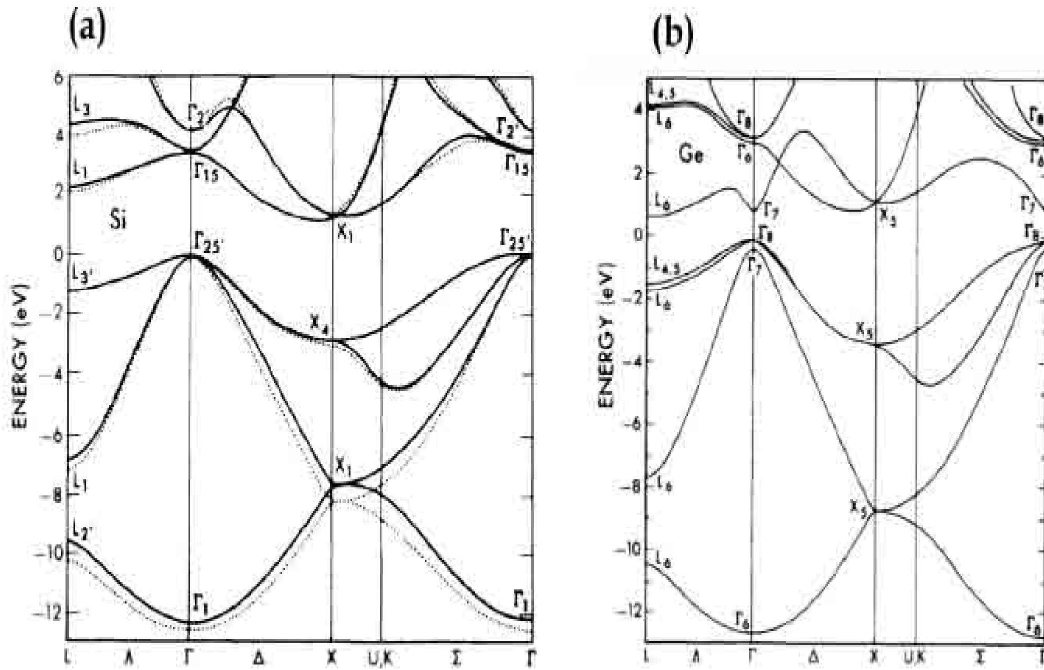

Figure 2-1 Band-diagram of (a) silicon and (b) germanium. Figure from [3].

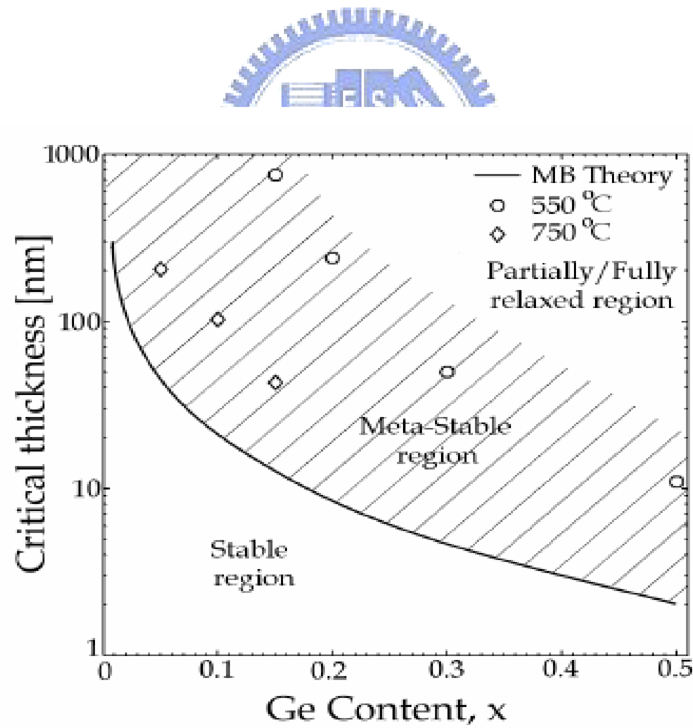

Figure 2-2 Experimental data of critical thickness for SiGe layers grown at 550 C (○) [2] and 750 C (◇) [4] with MB equilibrium calculated line.

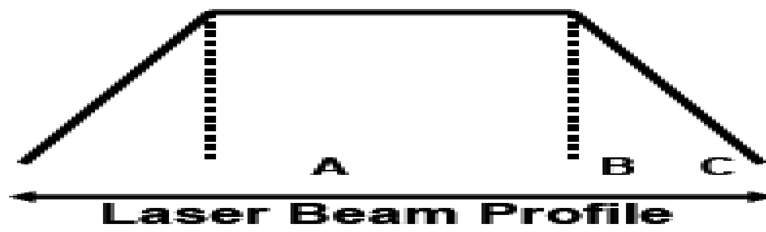

(a)

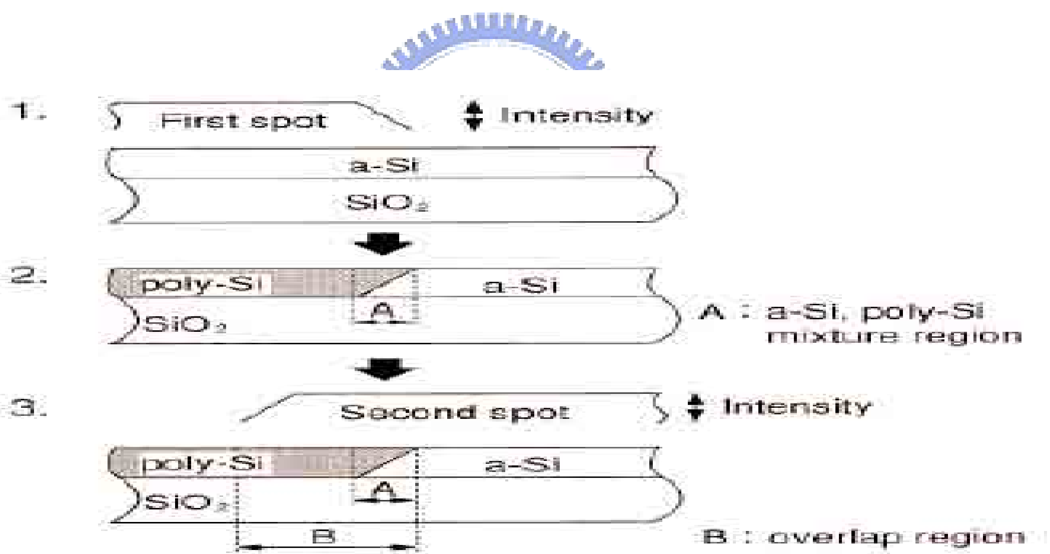

(b)

Figure 2-3 (a)Laser beam profile (b) conformity of overlapping and the deviation of each laser pulse

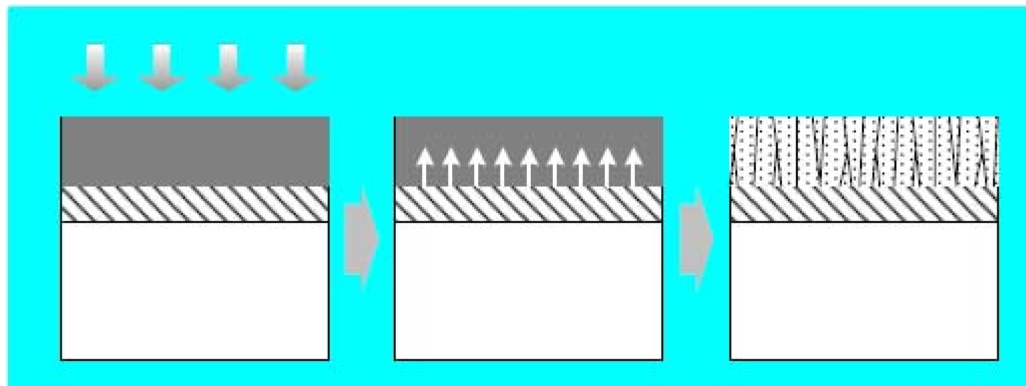

(a) partial melting

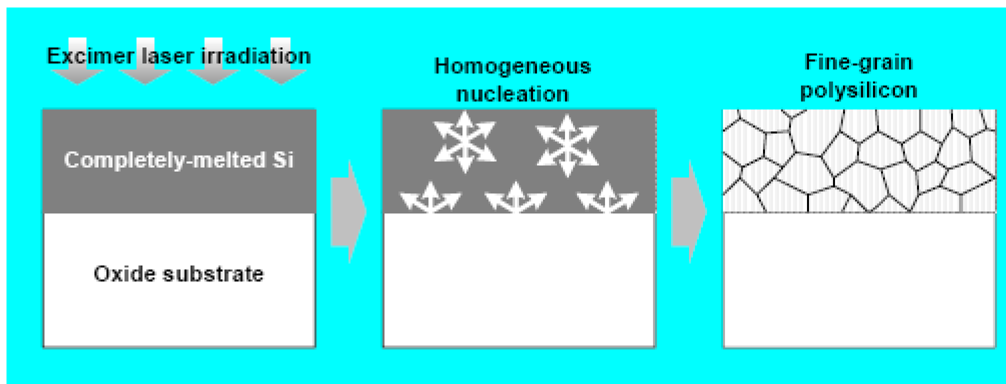

(b) complete melting

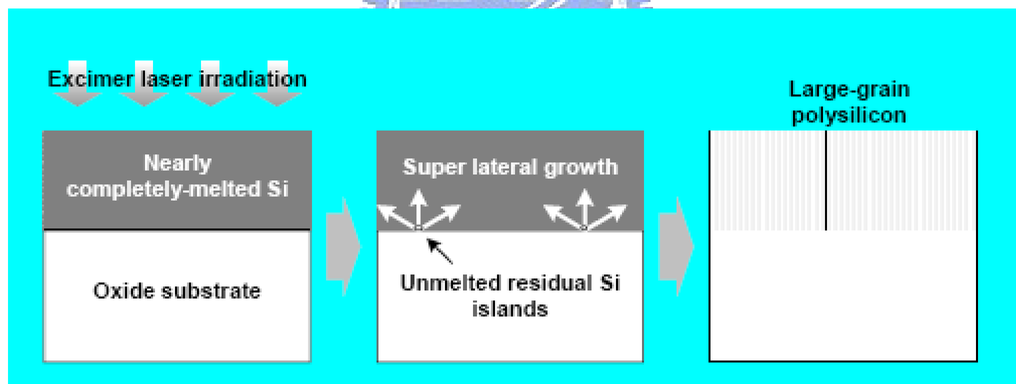

(c) nearly complete melting

Figure 2-4 Schematic diagrams of recrystallization mechanisms with respect to different energy density of ELA: (a) partial melting regime, (b) complete melting regime and (c) nearly complete melting (super lateral growth) regimes

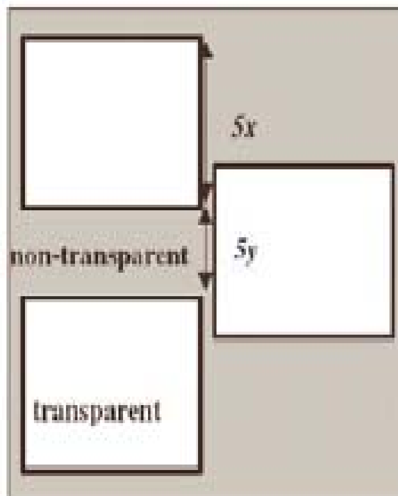

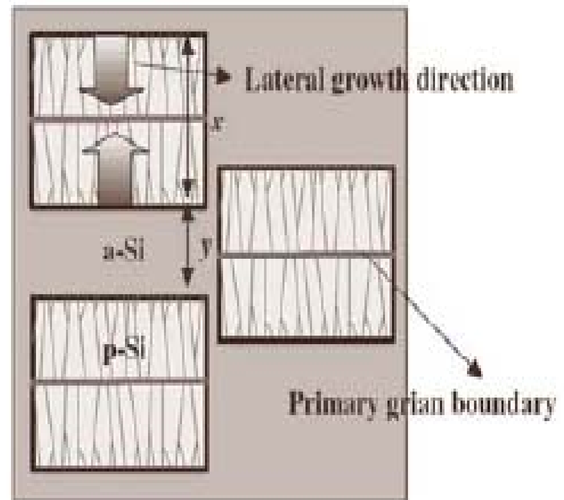

(a) Mask pattern (b) 1st shot irradiation

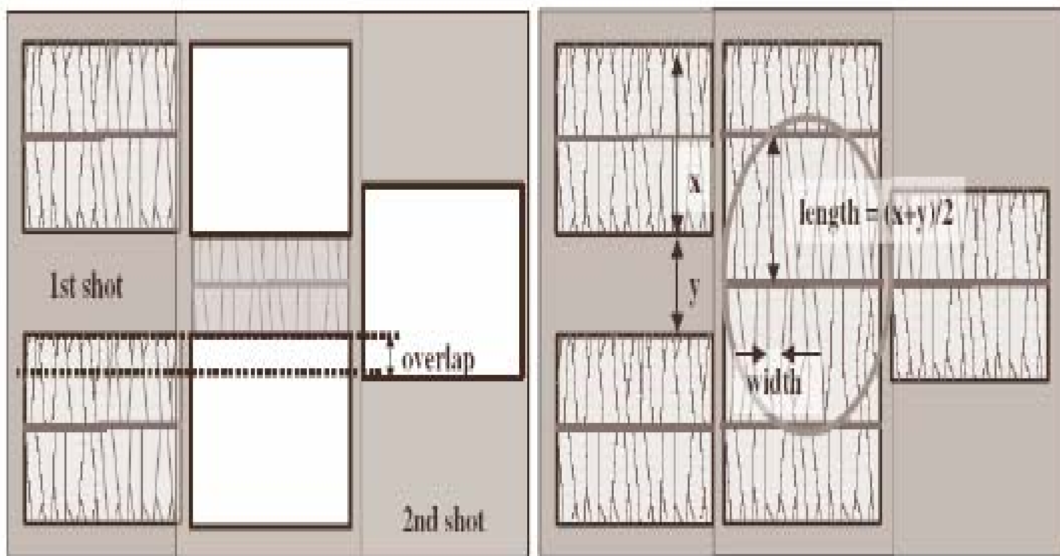

(C)Mask shift (d) 2st shot irradiation

Figure 2-5 (a) Mask pattern and (b) (c) (d) schematically show the microstructural evolution that results when SLS is carried out using a narrow line beamlet.

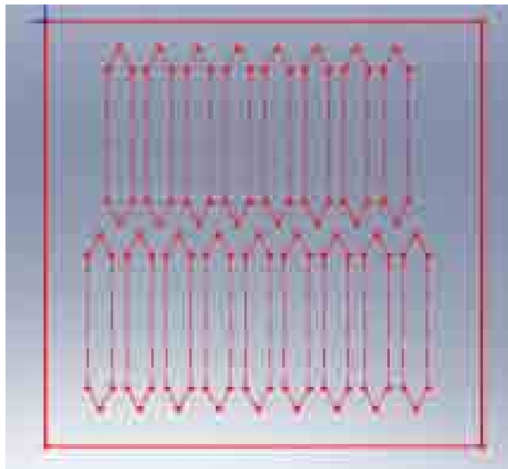

(a)

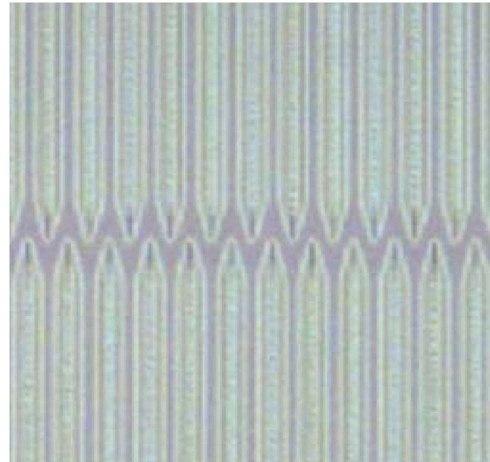

(b)

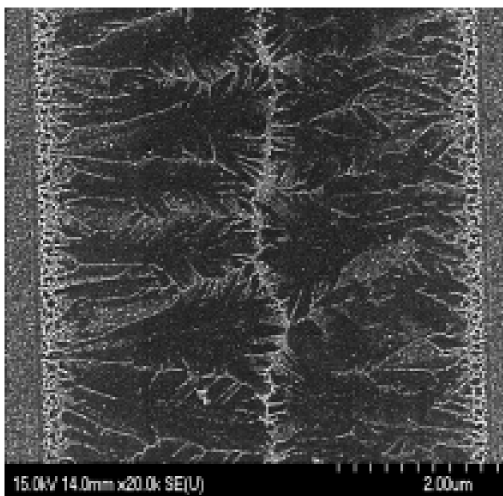

(c)

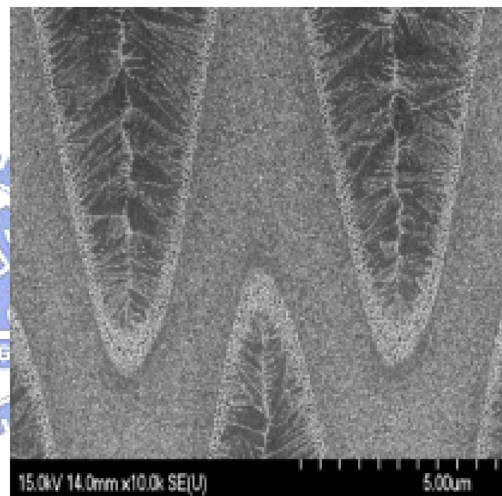

(d)

Figure 2-6 Optical micrographs of SLS-processed film: (a)Mask patten. (b)low magnification. Straight-slit + chevron-shaped beamlet. (c) High magnification. After Secco-Etched, Straight-slit beamlet (d) chevron-shaped beamlet .The dark-field with dotted lines demarking the boundaries between the single-crystal and columnar crystal region.

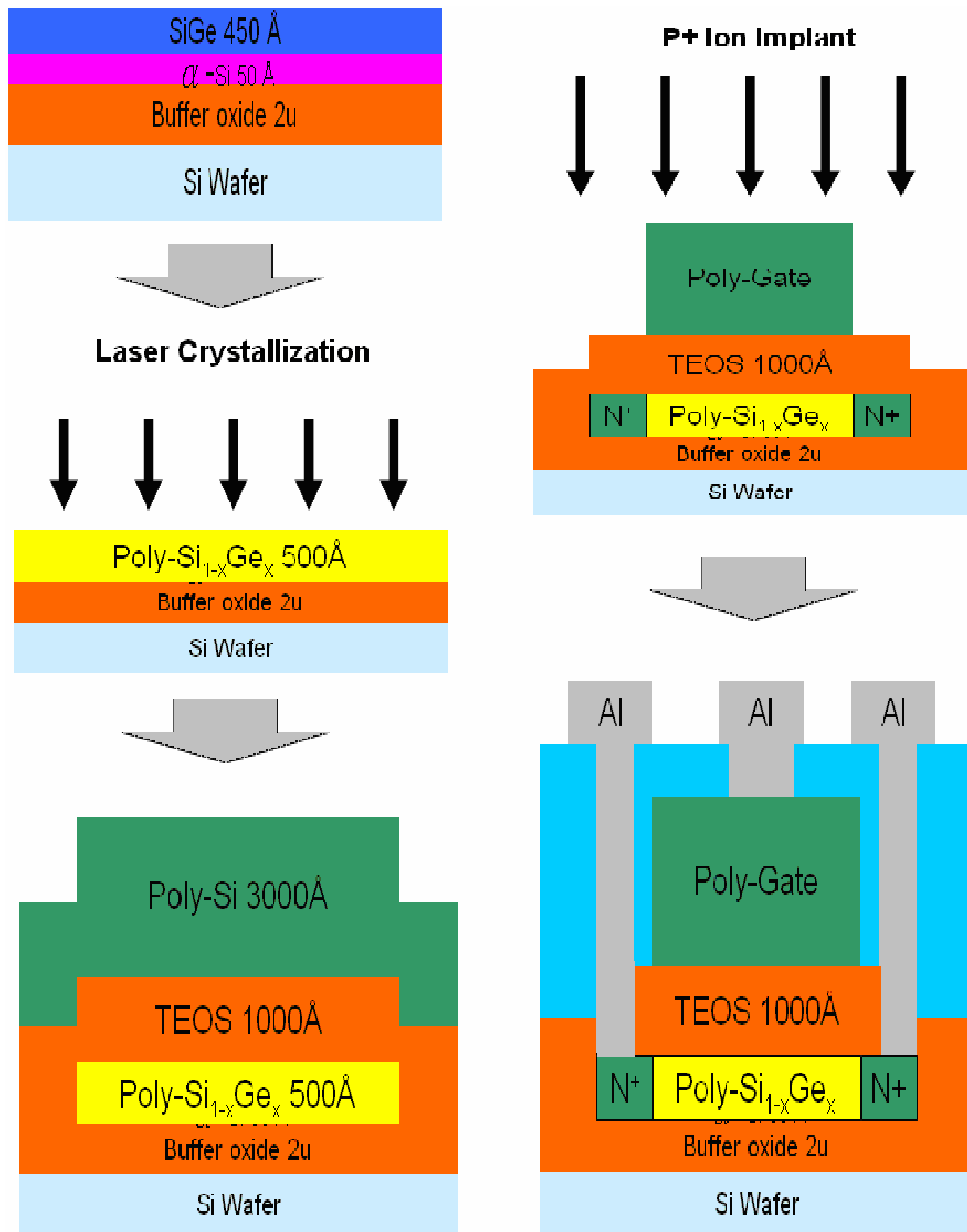

Figure 2-7 The key process procedure of fabricating SLS-Procssed poly-$Si_{1-x}Ge_x$ TFTs.

Chapter 3

Results and Discussion

3-1 Material Characterization of Super ateral-growth Crystallization of oly-$Si_{1-x}Ge_x$ Thin Films

3-1-1 Raman Spectroscopy Analysis

Raman spectroscopy is a contactless technique providing information about all these features in $Si_{1-x}Ge_x$ thin film with a high degree of experimental simplicity. It has been proven to be sensitive to the composition, stress and phonon correlation length. The crystalline volume fraction of the polycrystalline thin film can also be obtained from de-convoluting the Raman spectrum of the polycrystalline thin film into crystalline and amorphous components. Figure 3-1 is Raman spectra of thin films as deposited. Figure 3-2 - Figure 3-4 is the Raman spectra of the crystallized polycrystalline thin films irradiated with different laser energy at room temperature. As shown in these figures, the broad band of the as-deposited $Si_{1-x}Ge_x$ thin film represents no crystalline phase existing inside the film. In addition, the Raman peak intensity is weak due to the strong absorption coefficient of α-$Si_{1-x}Ge_x$ thin film at the wavelength of incident Raman laser beam. After excimer laser irradiation, the absorption coefficient of the poly-$Si_{1-x}Ge_x$ thin film decreased. Thus, the poly- $Si_{1-x}Ge_x$ thin film becomes more transparent.

Some representative Raman spectra of laser-crystallized poly- $Si_{1-x}Ge_x$ with x= 0.34, 0.5 are shown in Figure 3-3 and Figure 3-4. The spectrum in Figure 3-3 was obtained from a poly-$Si_{0.66}Ge_{0.34}$ sample that was crystallized with a laser energy of E_L=600,700,800 and 900 mJ/cm^2. The strongest phonon

line at 496.465 cm^{-1} originates from Si–Si lattice vibrations. The smaller peaks at 399.796 and 283.68 cm^{-1} are due to Si–Ge and Ge–Ge lattice vibrations, respectively. The weak peak at 421.35 cm^{-1} is also well known and is attributed to localized Si–Si vibrations surrounded by Ge atoms [3.1]. The spectrum in Figure 3-4 was obtained from a poly-$Si_{0.5}Ge_{0.5}$ sample that was crystallized with a laser energy of E_L=600,700,800 and 900 mJ/cm^2. Table 3-1 show the main Raman peak position (cm^{-1}). The sample crystallized exhibits a shoulder in the Si–Ge mode at about 399.796 cm^{-1} indicating that peak splitting takes place. It is important to note that the Ge–Ge and Si–Si modes are split too. It mean excimer laser crystallization of amorphous SiGe causes significant phase segregation and produces a polycrystalline alloy with Ge poor and Ge rich areas[3.2]. Figure 3-5 and Figure 3-6 (a) and (b) show the position of the phonon peaks that were obtained from the poly-$Si_{0.66}Ge_{0.34}$ and poly-$Si_{0.5}Ge_{0.5}$, respectively . Figure 3-6 (b) show the position of the 800 mJ/cm^2 phonon peaks is different the other laser energy phonon peaks. It clearly shows phase segregation.

The spectrum in Figure 3-7 - Figure 3-10 was obtained from the sample that was crystallized with a laser energy of E_L=600,700,800 and 900 mJ/cm^2, respectively. Each spectrum is characterized by three dominant peak centered near 300, 400, and 500 cm^{-1}. The fact that frequency dependence on x for both sets of samples is the same shows that former alloy layers are free of strain. The dependences of the Si-Si, Si-Ge, and Ge-Ge phonon frequencies on composition, *x*, and in-plane strain, ε, they proposed are reliable [3.3].

$$\omega_{SiSi} = 520.5 - 62x - 815\varepsilon \quad (1)$$

$$\omega_{SiGe} = 400.5 + 14.2x - 575\varepsilon \quad (2)$$

$$\omega_{GeGe} = 282.5 + 16x - 385\varepsilon \quad (3)$$

Hence, the knowledge of the phonon frequencies allows us to define three linear relationships between *x* and ε. We will exemplify the evaluation of *x* and ε for SiGe samples. By introducing the experimental frequencies of poly-$Si_{0.66}Ge_{0.34}$ into Eqs. (1)–(3), we obtain ε= 0.36%. For poly-$Si_{0.5}Ge_{0.5}$, we obtain ε= 0.89%. It clearly shows the strain almost relax.

3-1-2 Scanning Electron Microscope (SEM) Analysis

Theα- Si, α- $Si_{0.66}Ge_{0.34}$, andα- $Si_{0.5}Ge_{0.5}$ films were crystallized using 600, 700, 800, and 900 mJ/cm^2 Laser Energy at an optimal laser fluence for each set of conditions shown in Table 3-2. For device applications, the structure properties of the poly-Si thin films are of major interest. The primary concerns are the grain size, quality of the grains, and the grain size distribution, and these properties will strongly influence the electrical characteristics of TFT. In this work, the average grain size of the SLS-processed poly- $Si_{1-x}Ge_x$ thin film is measured by using scanning electron microscopy (SEM). In order to distinguish the individual grain structure, before observation, the SLS-processed poly- $Si_{1-x}Ge_x$ thin films are etched by using the Secco etching, which etched the grain boundaries more quickly than the interior parts of the grains. Figure3-11 ~ Figure 3-13 shows the SEM micrographs of the SLS-processed poly-$Si_{1-x}Ge_x$ film after Secco etching. The excimer laser energy densities are adjusted to partially or completely melt the a- $Si_{1-x}Ge_x$ thin film. As shown in Figure 3-11 ~ Figure 3-13, distinguishable grains and grain boundaries are observed, EDS analyses, it has been found that serious grain boundary Ge segregation occurs after excimer laser irradiation. The grain boundary regions may be the segregated Ge-rich poly-$Si_{1-x}Ge_x$ because the

Secco etching solution is proven to be unable to etch the Ge-rich poly-$Si_{1-x}Ge_x$ thin film. This provides evidence that Ge atoms segregate toward the grain boundaries in the SLS-processed poly-$Si_{1-x}Ge_x$ thin film.

According to Figure 3-11 ~ Figure 3-13, fine-grained material at the periphery of the molten zone induces lateral growth of solid material toward the center. This leads to super-lateral growth of the solid material into the super-cooled liquid that proceeds until one of two possible outcomes takes place[3-1]; 1. the growth fronts from opposing sides of the molten zone impinge upon one another at the center, or 2. the liquid cools below a temperature at which nucleation is more probable and the formation of fine-grain material halts the lateral growth. The shape of the grains results from the formation at the periphery of the molten zone, all of which initiate lateral growth into the super-cooled liquid, as show in Figure 3-14. The former of the two possible outcomes is preferred, as this prevents fine-grained material from forming within the center of the crystallized area, as show in Figure 3-16. The middle region due to Ge-rich and Ge-poor lattice parameter mismatch to make strain. When strain is large, the broken lattice parameter will relaxation the strain, as show in Figure 3-15.

3-1-3 Atomic Force Microscopy (AFM) Analysis

The shapes and sizes of the islands have been determined by means of atomic force microscopy (AFM). AFM pictures of samples poly-Si, poly-$Si_{0.66}Ge_{0.34}$ and poly-$Si_{0.5}Ge_{0.5}$ are shown in Figure 3-17- Figure 3-19. The grains can reach the center of the molten line, it clearly shows that increase Ge concentration the grain peak will be increase.

3-1-4 Energy Dispersive X-ray(EDS) Analysis

Figure 3-20 displays the SEM images of the laser-crystallized poly-$Si_{0.66}Ge_{0.34}$ and aser-crystallized poly-$Si_{0.5}Ge_{0.5}$ thin film. The energy dispersive X- ray (EDX) analysis was used to verify the atomic composition existing across the SiGe thin film. The EDX results indicated that the Ge atomic concentration near the grain boundary is higher than that in the middle of the film after excimer laser irradiation. Figure 3-21 and Figure 3-22 displays the EDX analysis results of different laserenergy and Ge concentration, respectively. By grading the Ge content across the grain, the band gap will be different as shown Figure 3-23.

3-2 The Crystallization Mechanism of SLS-Procssed α-$Si_{1-x}Ge_x$ Thin Films

According to the material analysis results shown above, the phenomenon of Ge segregation at grain boundary. Here a new crystallization mechanism suitable for the SLS-processed poly-$Si_{1-x}Ge_x$ thin films is proposed. Figure 3-24 illustrates the proposed crystallization model for poly-$Si_{1-x}Ge_x$ films crystallized by SLS-processing. At the solid/liquid interface the molten alloy starts to solidify and grains grow towards the interference maximum, along the thermal gradient. At the line of maximum intensity, the grains meet with grains growing from the other side and form a grain boundary. By grading the Ge content across the grain, the most possible reason responsible for the Ge segregation is the difference in melting point of these two atoms, Si and Ge. The melting temperatures of Si and Ge atoms are 1410℃ and 936℃, respectively. Due to the difference of the melting point of Si and Ge atoms, the

melting Ge atoms will be driven to progress toward the liquid-solid interface during the initial solidification of $Si_{1-x}Ge_x$ thin film because at this moment the temperature of the $Si_{1-x}Ge_x$ thin film still maintains at the latent heat temperature, which is higher than the melting point of Ge atoms. And then, the un-solidified Ge atoms diffuse along with the propagation of the liquid-solid interface. When solidification process terminate, the Ge atoms also solidify and segregate at the last-solidified regions, where are the grain boundary. As a result, high Ge atomic concentration is observed at the grain boundary.

3-3 Electrical Characterization of SLS-Procssed poly-$Si_{1-x}Ge_x$ TFTs

For device applications, the structural properties of the poly- $Si_{1-x}Ge_x$ thin film are of major interest. These properties have a profound influence on the electrical characteristics of the fabricated poly- $Si_{1-x}Ge_x$ TFTs. Unfortunately, the device has death after open contact hole. Figure 3-25 and Figure 3-26 display the typical transfer characteristics of n-channel poly-$Si_{0.66}Ge_{0.34}$ TFTs fabricated by SLS-processing with device dimension (W/L = 10μm/10μm) before contact hole opened. Although the device has death but a trend can be observed.

An important anomaly behavior is the kink effect, a sudden rise in the drain current at a certain drain-to-source voltage that results in high drain conductance , leading to reduced voltage gain and poor linearity. The source of the kink is an issue of considerable contention at this time. Conventional experiment suggest that traps cause the kink: high fields charge traps in the buffer or in the insulator, leading to a shift in threshold voltage and poor

linearity. To improve floating body effect is a solution to control the kink effect. Thin films of poly-SiGe has lower valence band than poly-Si. The Ge-rich region has lower valence band than Ge-poor region. If the Ge-rich region at the source, the floating body effect will be improve by accelerate the hole emission. Figure 3-27 illustrates the proposed model for improving floating body effect.

Raman shift (cm^{-1})

	$Si_{0.66}Ge_{0.34}$				
	As Deposited	600mJ/cm^{-2}	700mJ/cm^{-2}	800mJ/cm^{-2}	900mJ/cm^{-2}
Ge-Ge	272.714	280.026	280.026	283.68	283.68
Si-Ge	399.763	399.763	399.763	399.763	399.763
Si_{loc}	421.35	435.71	428.533	421.35	417.757
Si-Si	492.904	496.465	496.465	496.465	496.465

	$Si_{0.5}Ge_{0.5}$				
	As Deposited	600mJ/cm^{-2}	700mJ/cm-^{2}	800mJ/cm^{-2}	900mJ/cm^{-2}
Ge-Ge	280.026	283.68	283.68	283.68	283.68
Si-Ge	396.16	399.763	399.763	399.763	399.76
Si_{loc}	435.71	421.35	421.35	421.35	421.35
Si-Si	478.642	482.21	482.21	485.776	482.21

Table 3-1 Raman peak position (cm^{-1})

Initial T/F / Laser Energy	α-Si	α-$Si_{0.66}Ge_{0.34}$	α-$Si_{0.5}Ge_{0.5}$
600mJ/cm2	**Nucleation occurred at inner region**	**Full**	**Full**
700mJ/cm2	**Full**	**Full**	**Full**
800mJ/cm2	**Full**	**Full**	**Full**
900mJ/cm2	**Full**	**Full**	**Broken**

Table 3-2 The material characteristic of the thin films laser crystallization with different laser energy

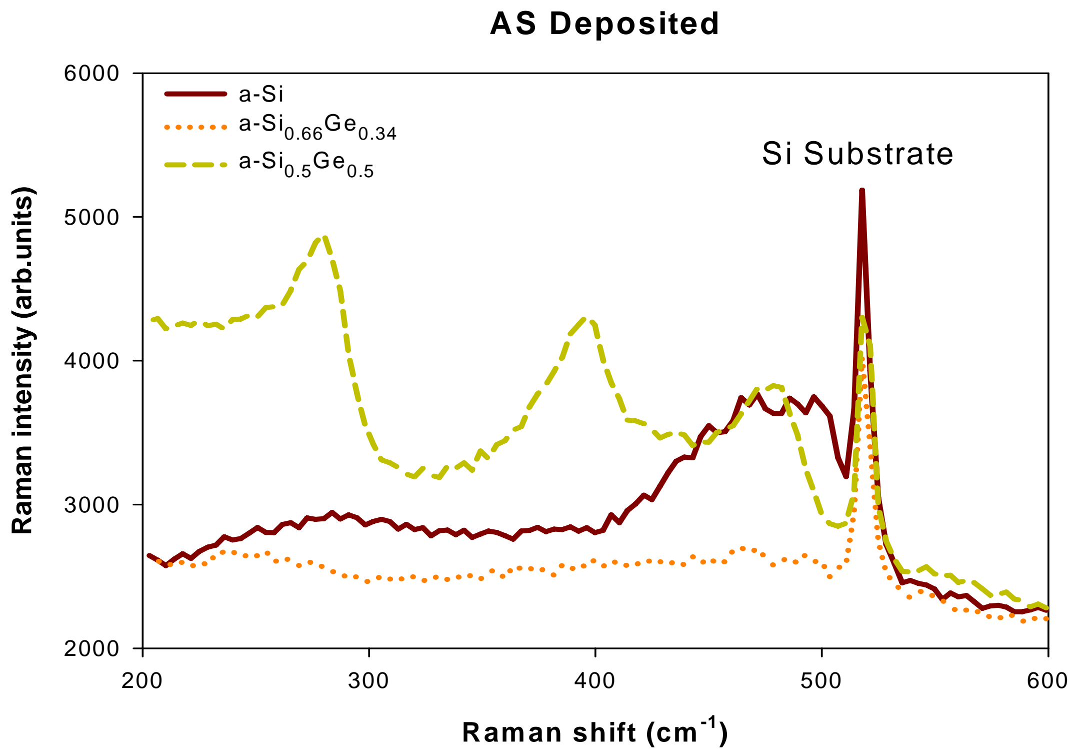

Figure 3-1 Raman spectra of thin films as deposited

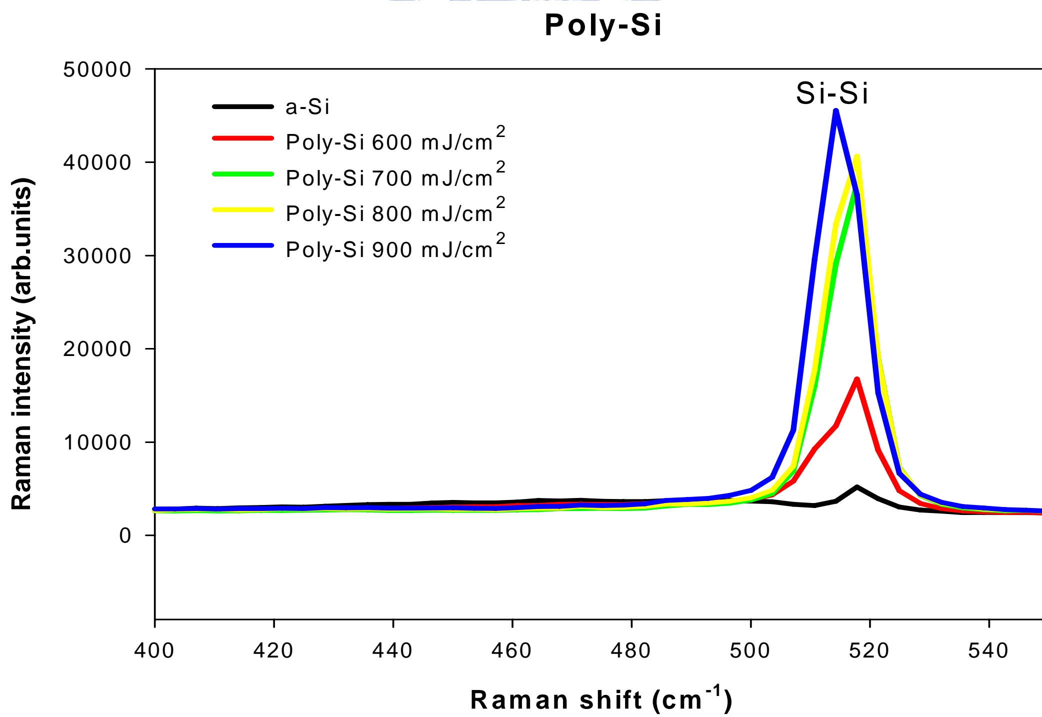

Figure 3-2 Raman spectra of SLS-processed Si thin films irradiated with different laser energy density at room temperature

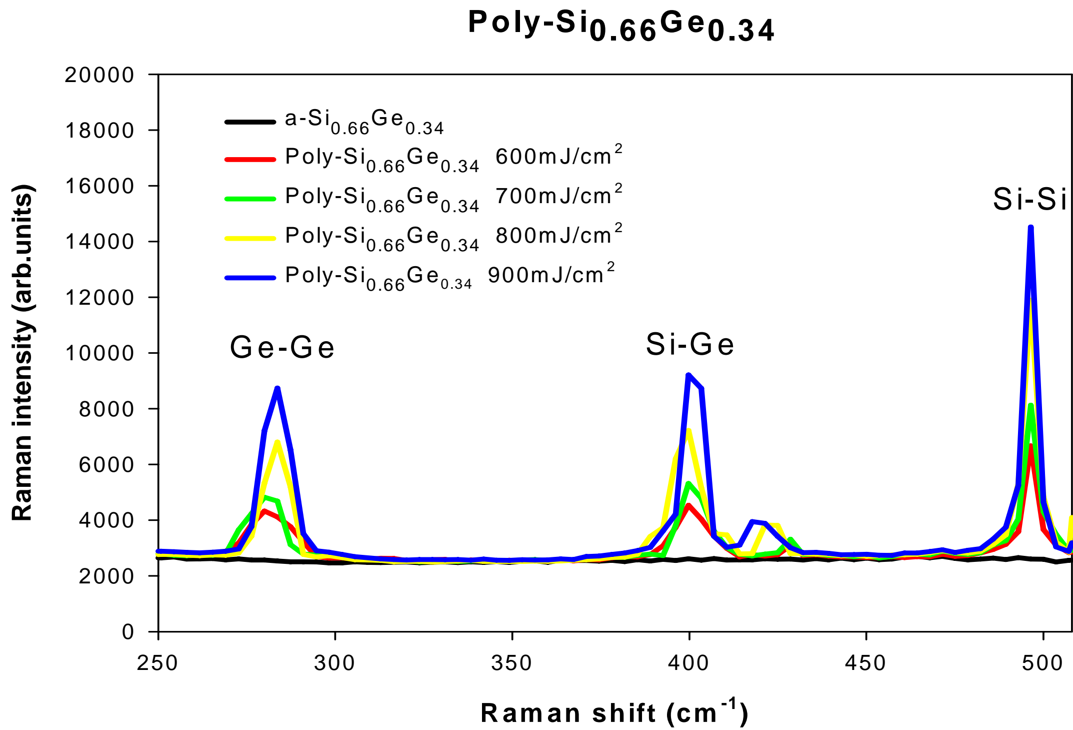

Figure 3-3 Raman spectra of SLS-processed $Si_{0.66}Ge_{0.34}$ thin films irradiated with different laser energy density at room temperature.

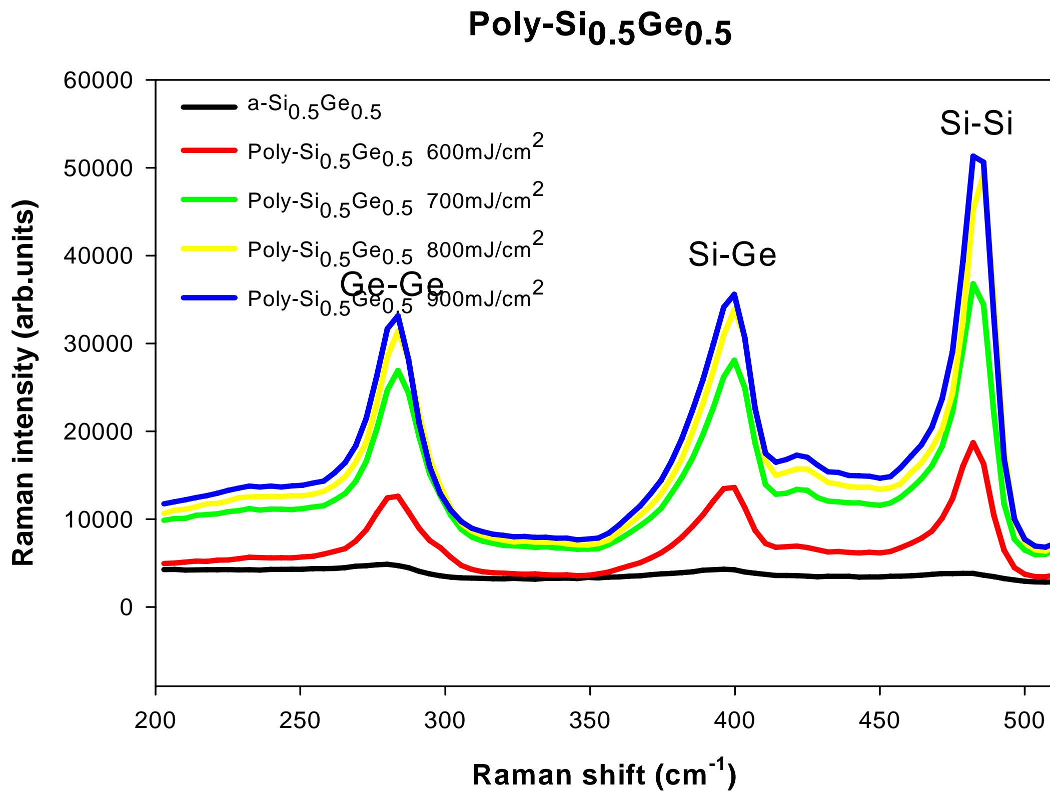

Figure 3-4 Raman spectra of SLS-processed $Si_{0.5}Ge_{0.5}$ thin films irradiated with different laser energy density at room temperature.

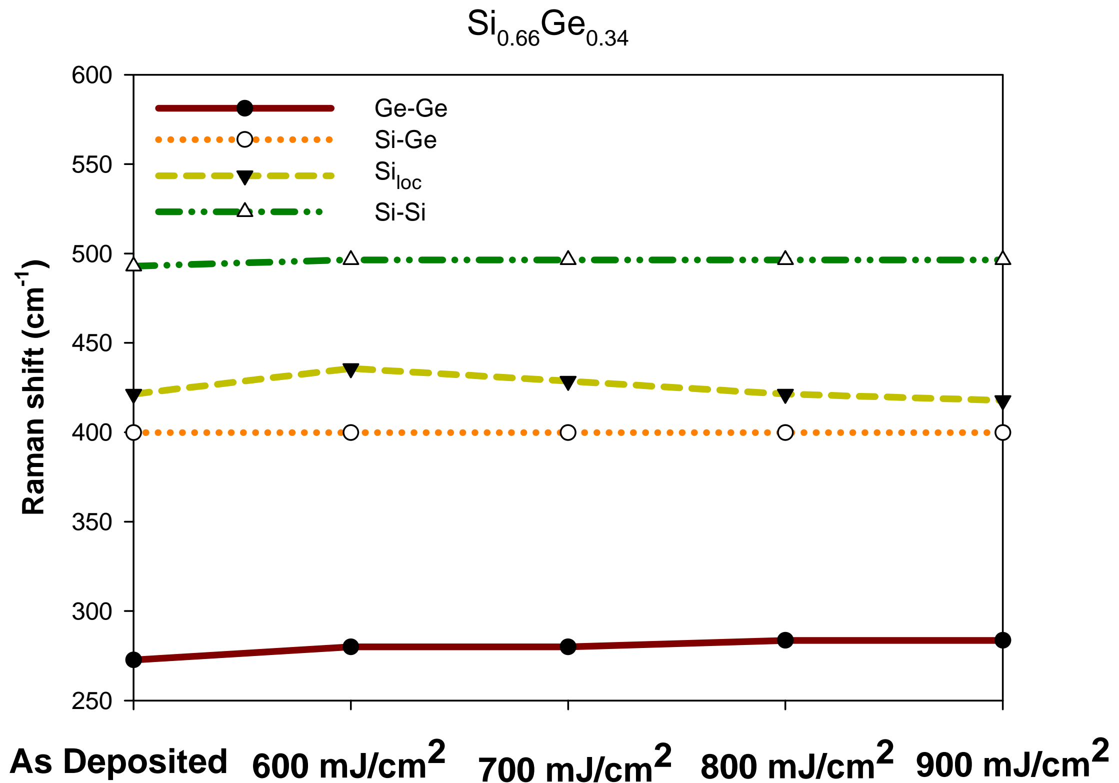

(a)

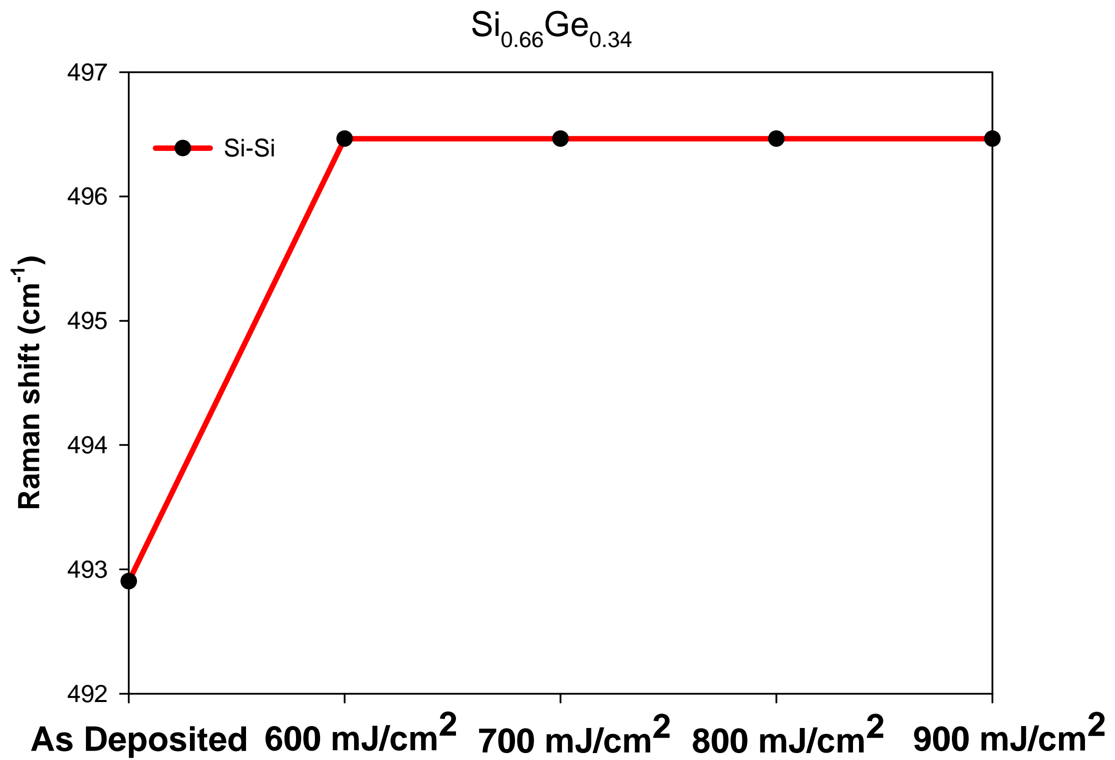

(b)

Figure 3.5 (a) The position of the Raman spectra of $Si_{0.66}Ge_{0.3}$ for 600,700,800 and 900 mJ/cm^2 (b)The line shows the position of the Si-Si mode in crystalline $Si_{0.66}Ge_{0.34}$.

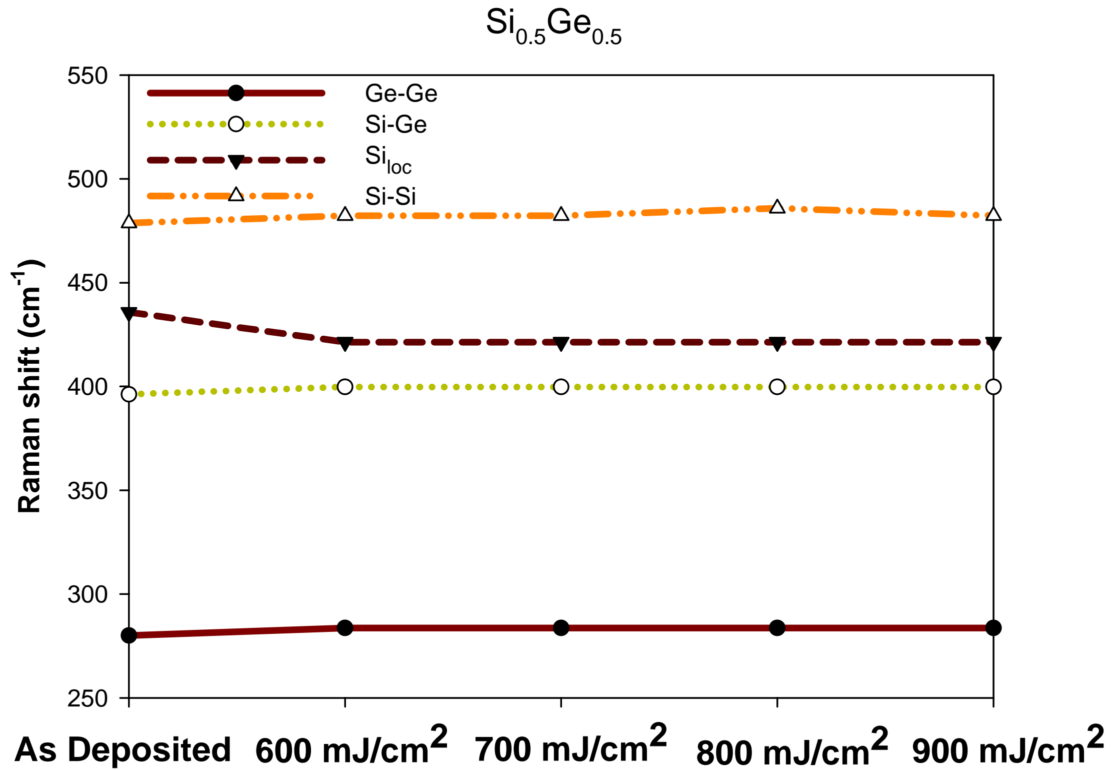

(a)

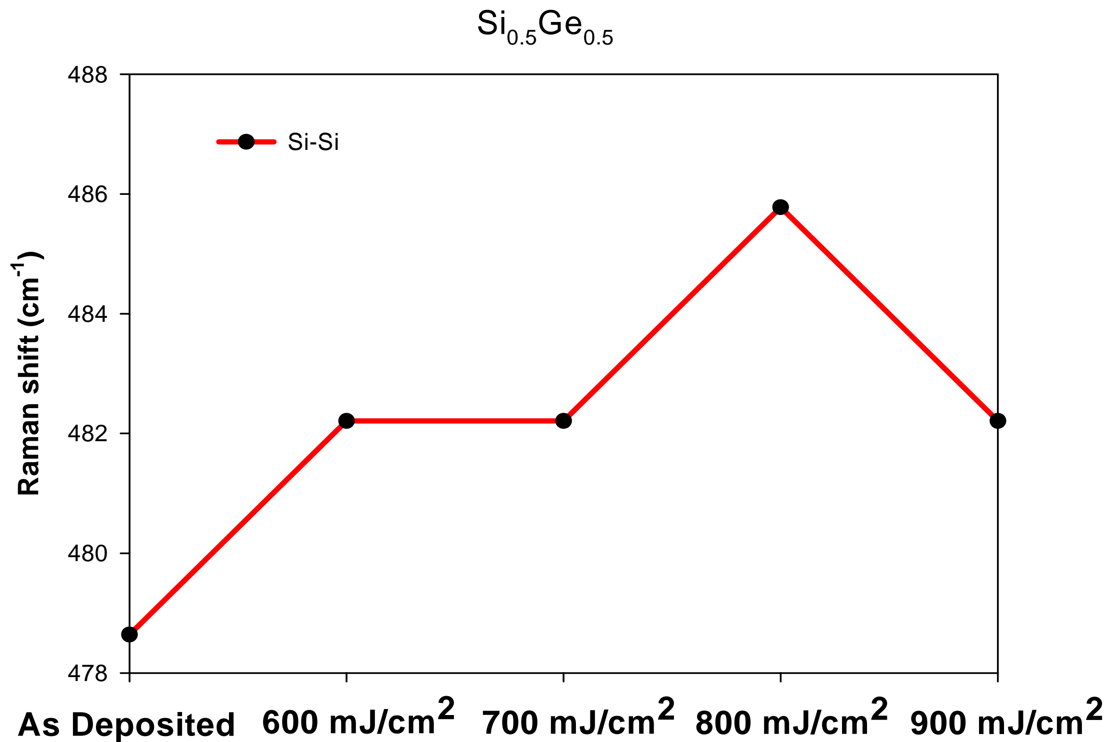

(b)

Figure 3-6 (a) The position of the Raman spectra of $Si_{0.5}Ge_{0.5}$ for 600,700,800 and 900 mJ/cm^2 (b)The line shows the position of the Si-Si mode in crystalline $Si_{0.5}Ge_{0.5}$.

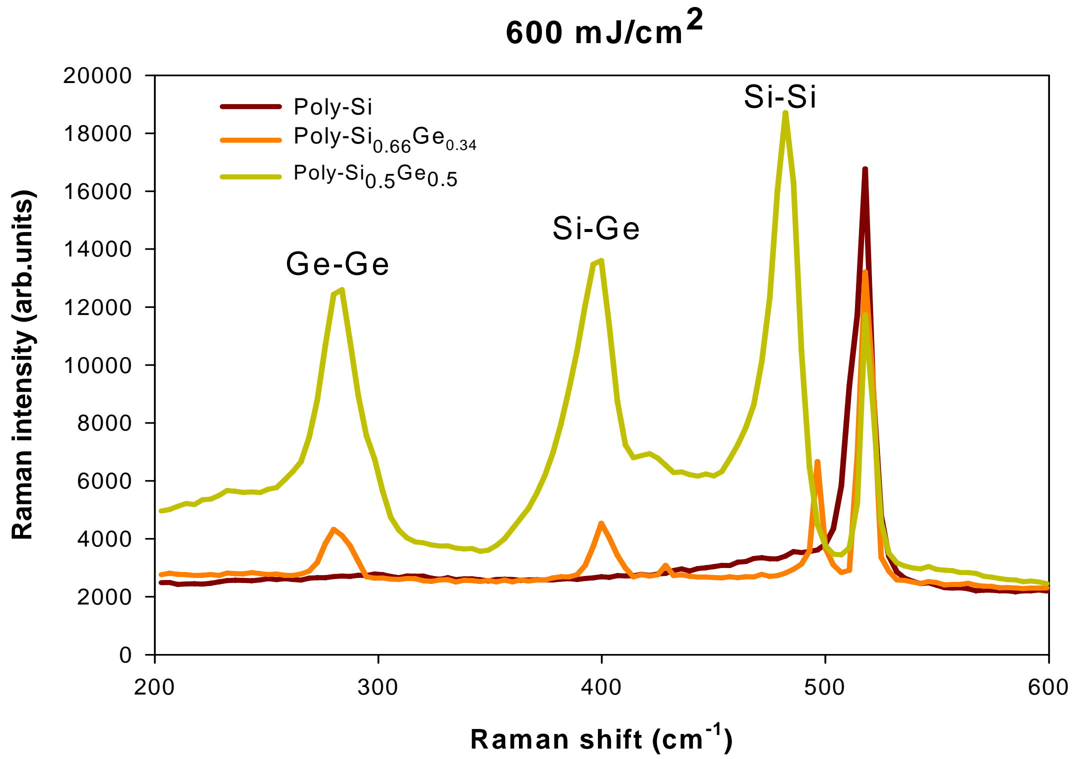

Figure 3-7 Raman spectra of SLS-processed thin films irradiated with 600 mJ/cm^2 laser energy density at room temperature

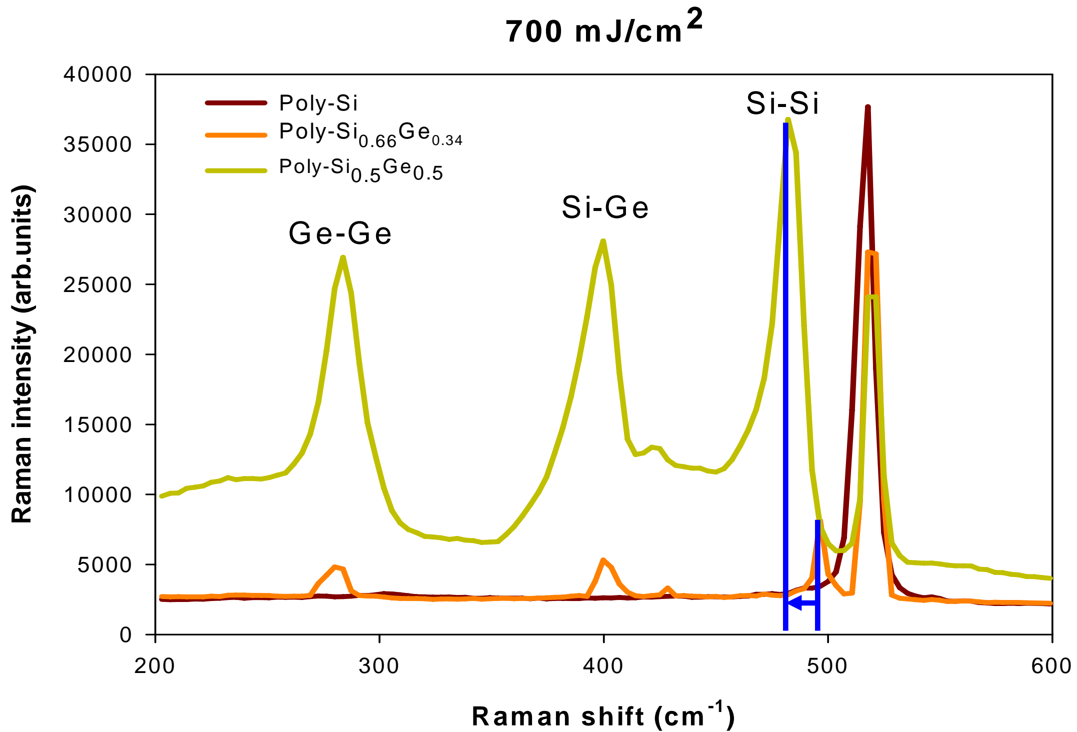

Figure 3-8 Raman spectra of SLS-processed thin films irradiated with 700 mJ/cm^2 laser energy density at room temperature

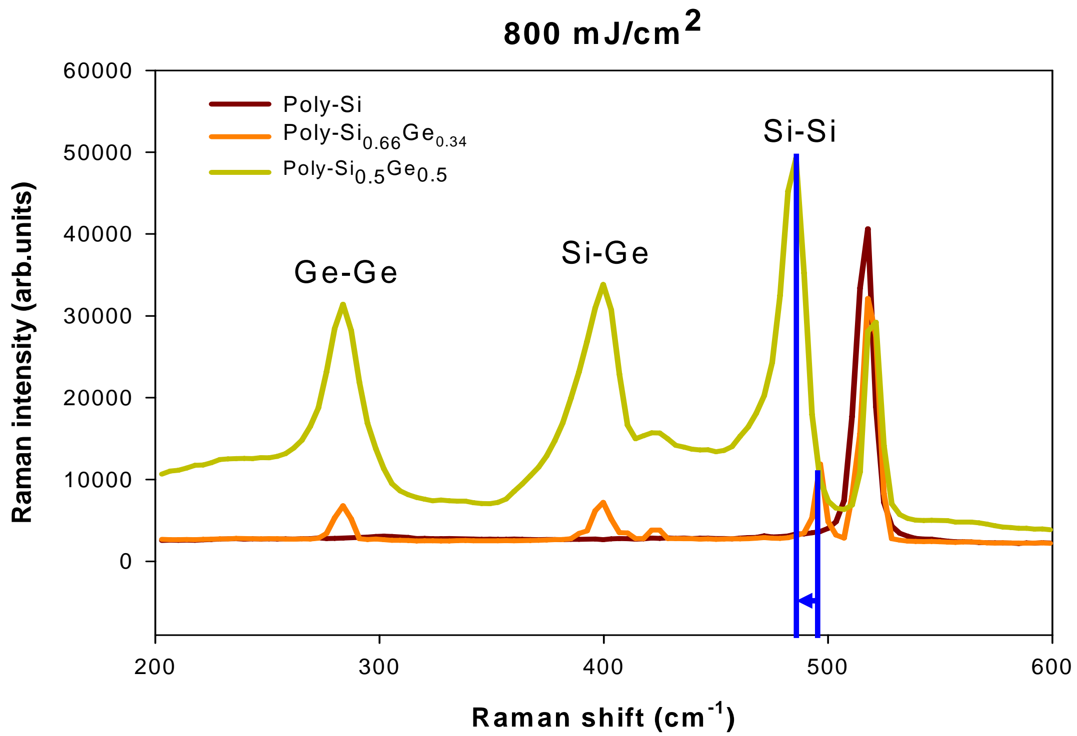

Figure 3-9 Raman spectra of SLS-processed thin films irradiated with 800 mJ/cm^2 laser energy density at room temperature

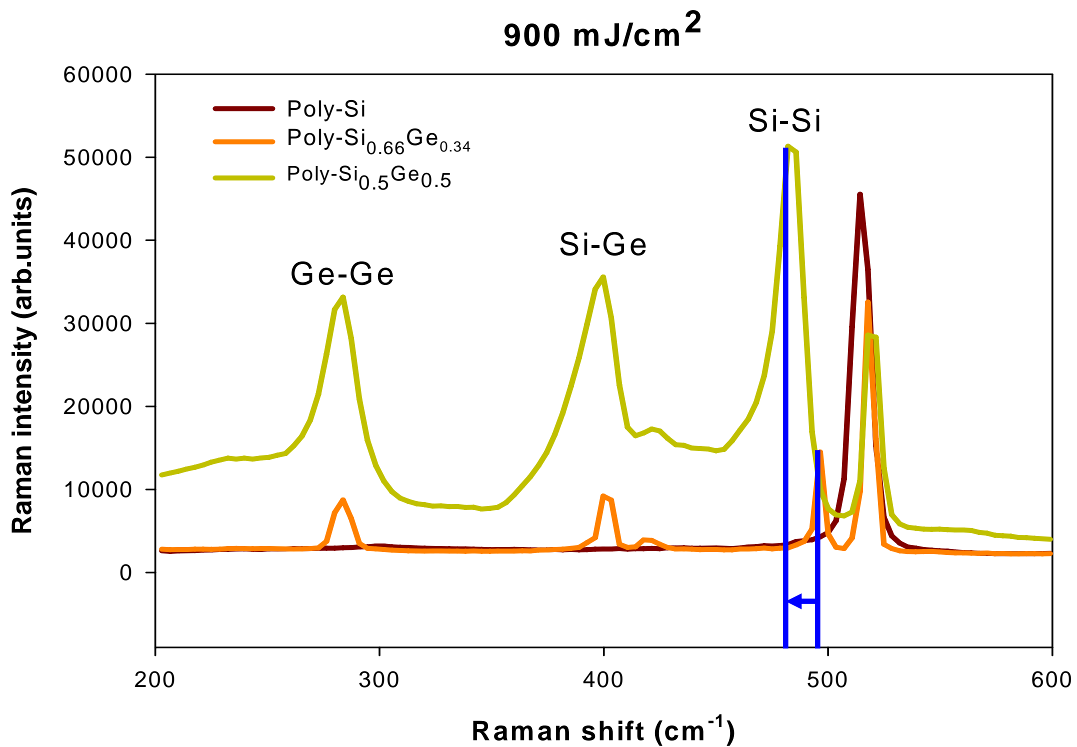

Figure 3-10 Raman spectra of SLS-processed thin films irradiated with 900 mJ/cm^2 laser energy density at room temperature

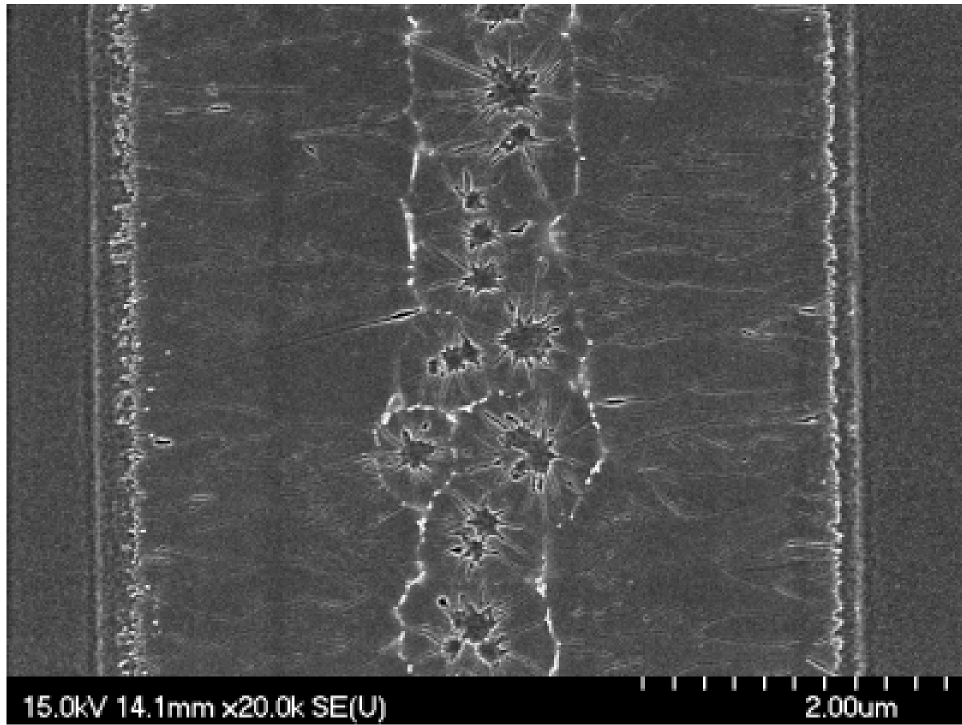

(a) Poly-Si　600mJ/cm^2

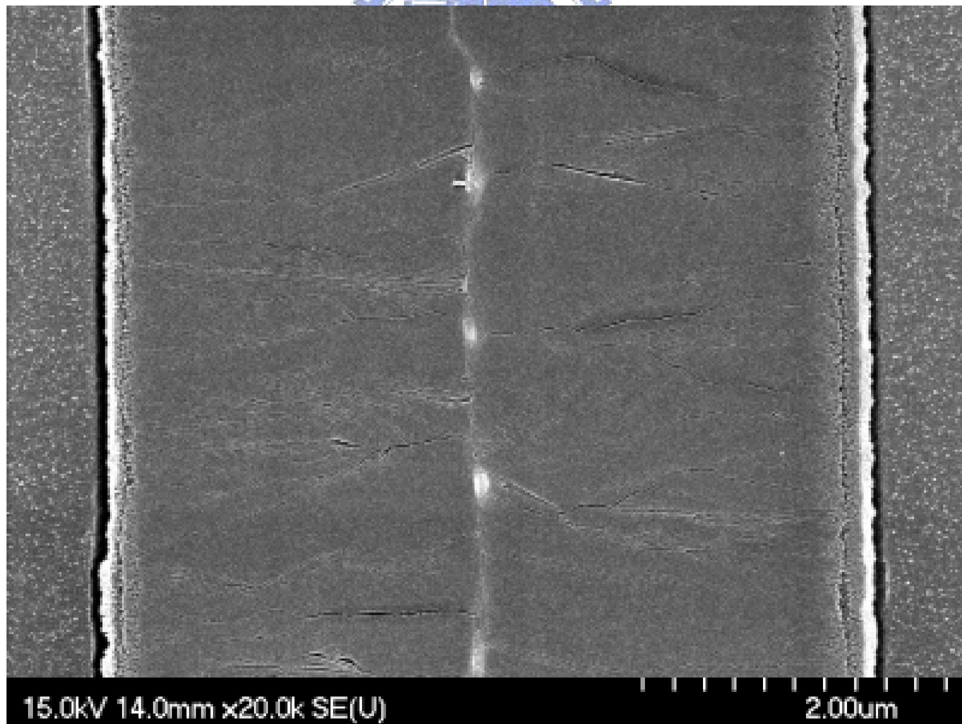

(b) Poly-Si　700mJ/cm^2

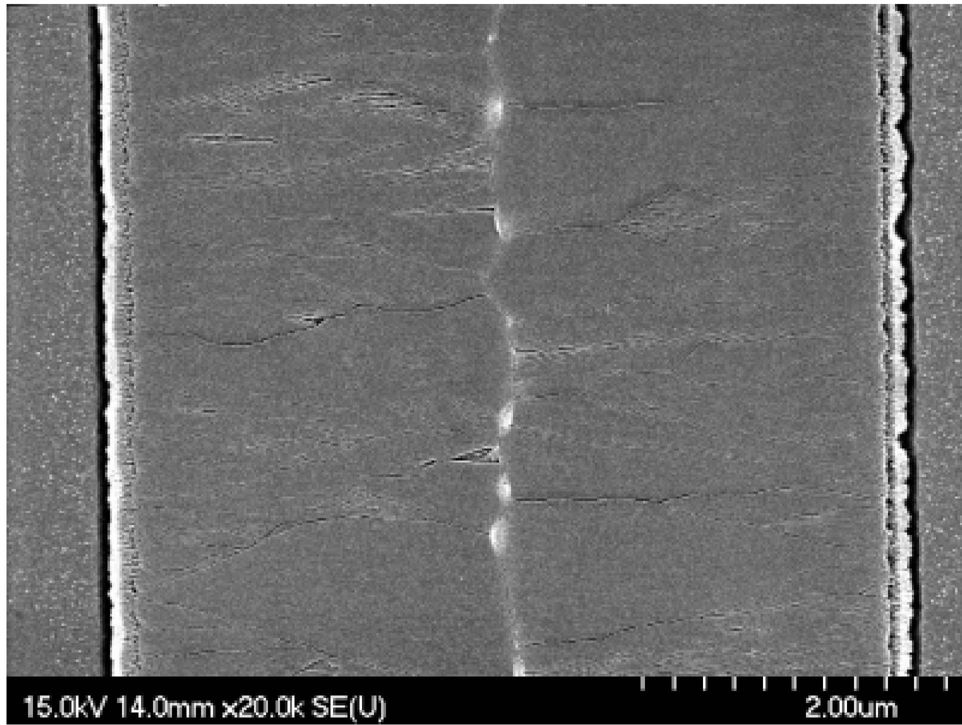

(c) Poly-Si 800mJ/cm^2

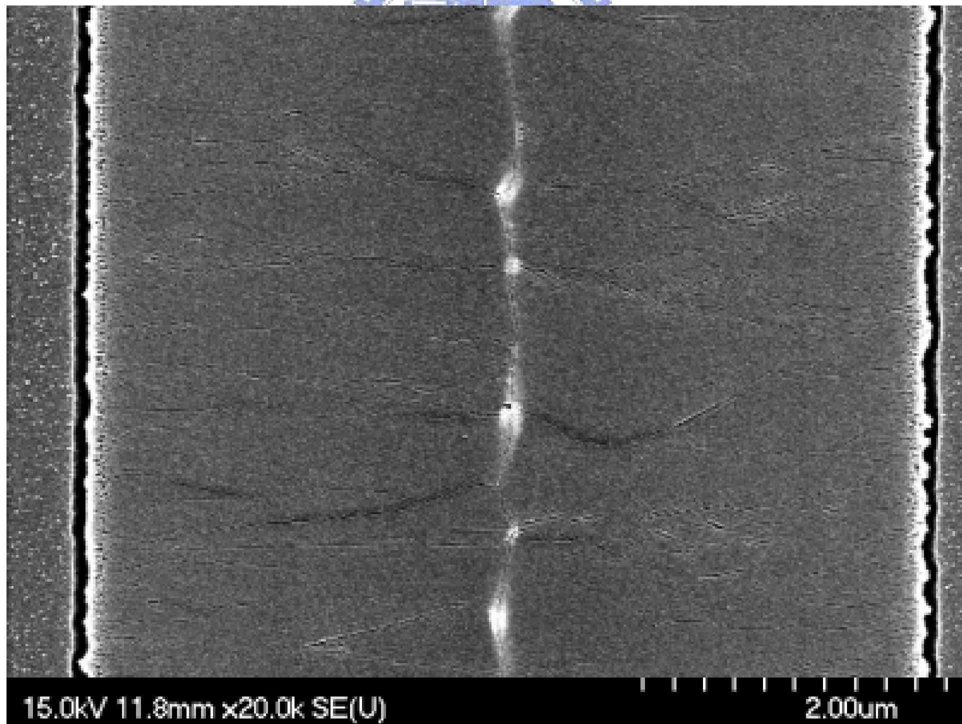

(d) Poly-Si 900mJ/cm^2

Figure 3-11α-Si Laser Crystallization after Secco etching

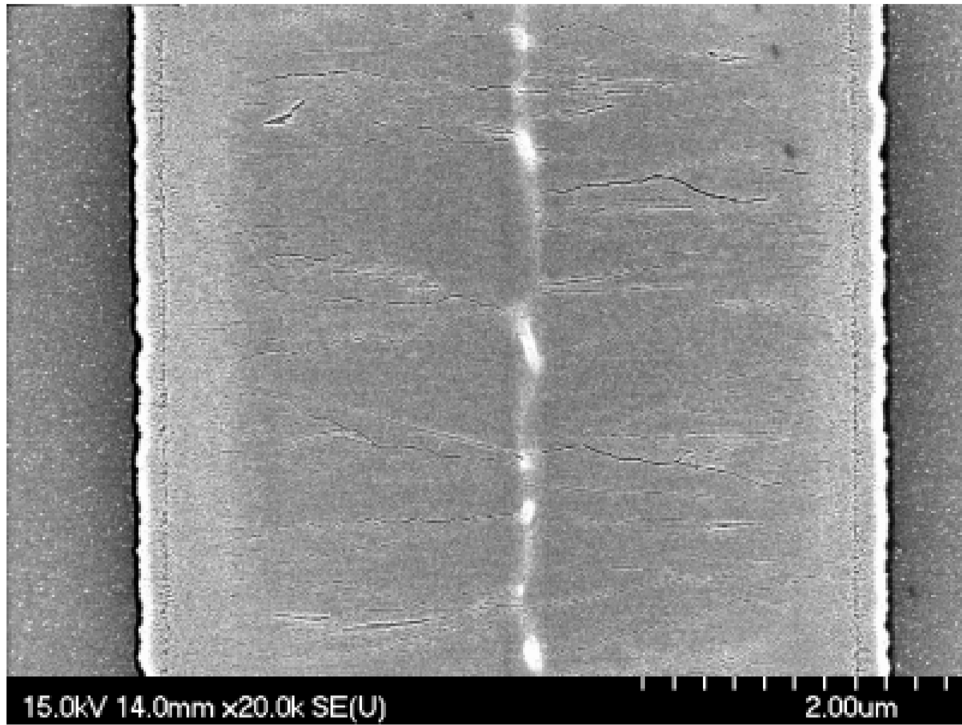

(a) Poly-$Si_{0.66}Ge_{0.34}$ 600mJ/cm^2

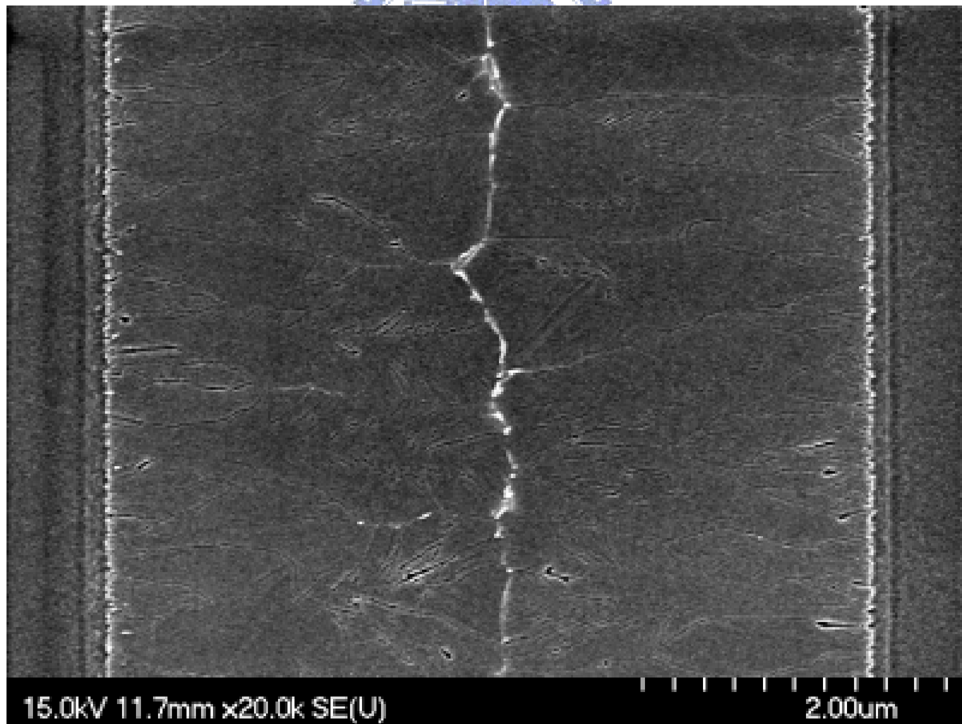

(b) Poly-$Si_{0.66}Ge_{0.34}$ 700mJ/cm^2

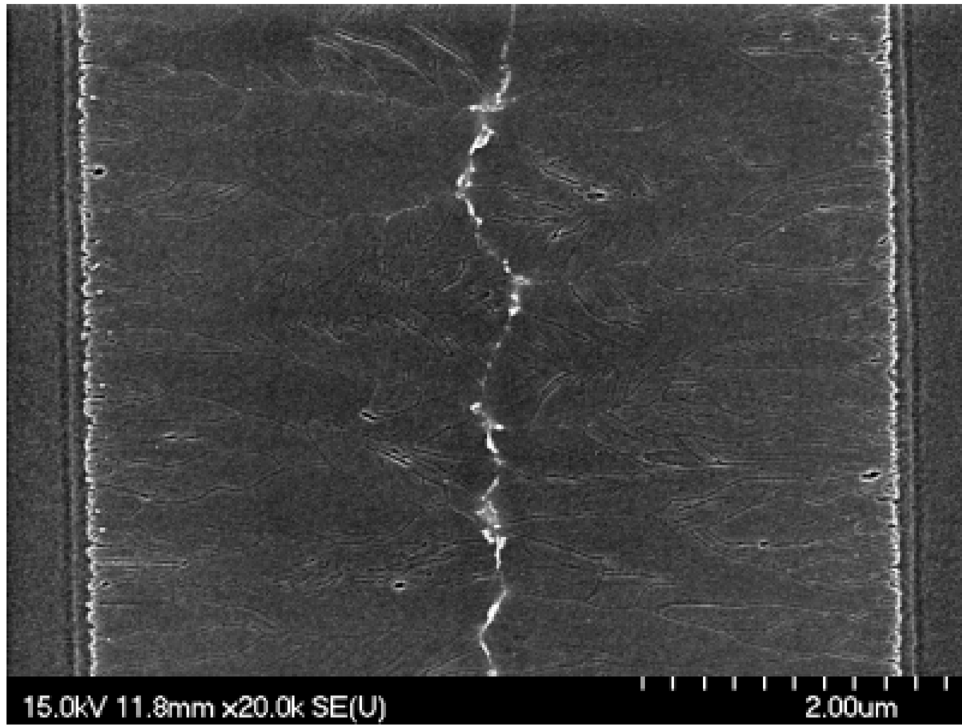

(c) Poly-$Si_{0.66}Ge_{0.34}$ 800mJ/cm^2

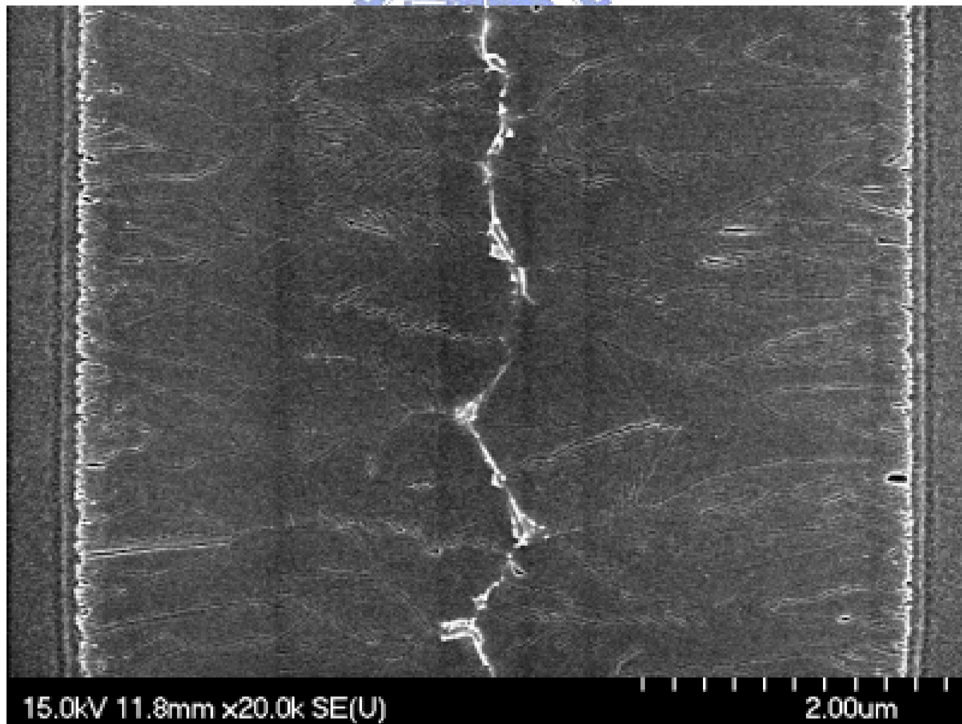

(d) Poly-$Si_{0.66}Ge_{0.34}$ 900mJ/cm^2

Figure 3-12α- $Si_{0.66}Ge_{0.34}$ Laser Crystallization after Secco etching

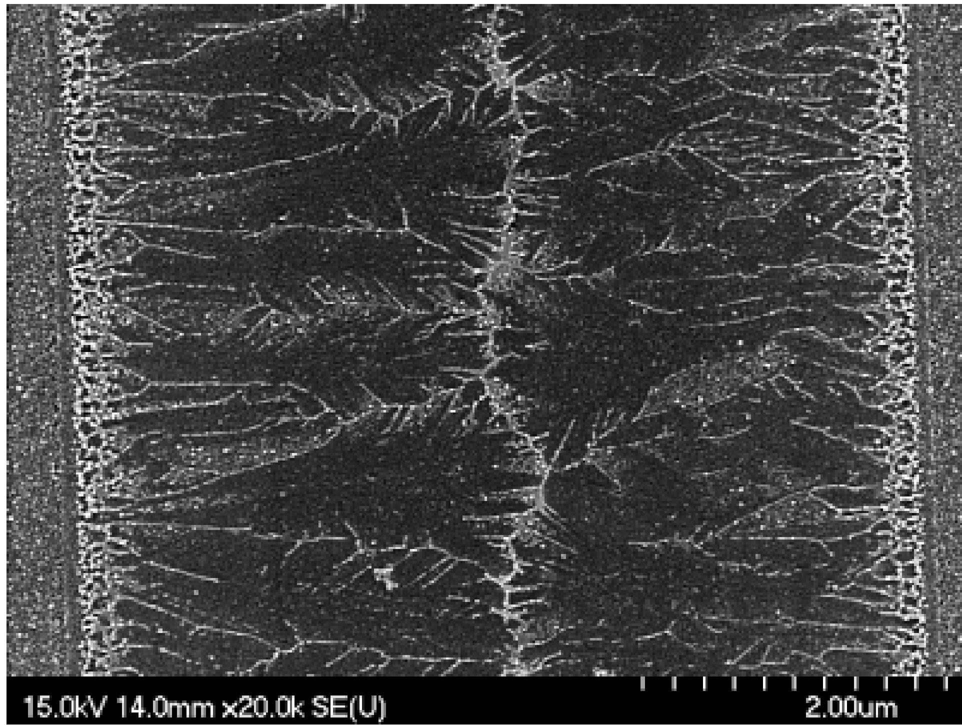

(a) Poly-$Si_{0.5}Ge_{0.5}$ 600mJ/cm^2

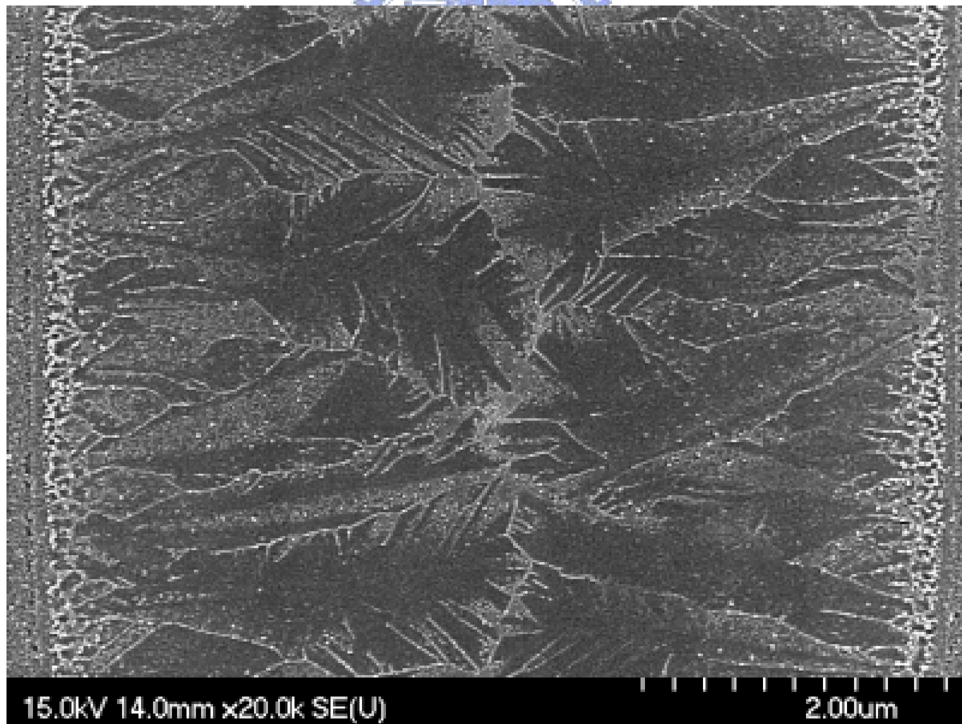

(b) Poly-$Si_{0.5}Ge_{0.5}$ 700mJ/cm^2

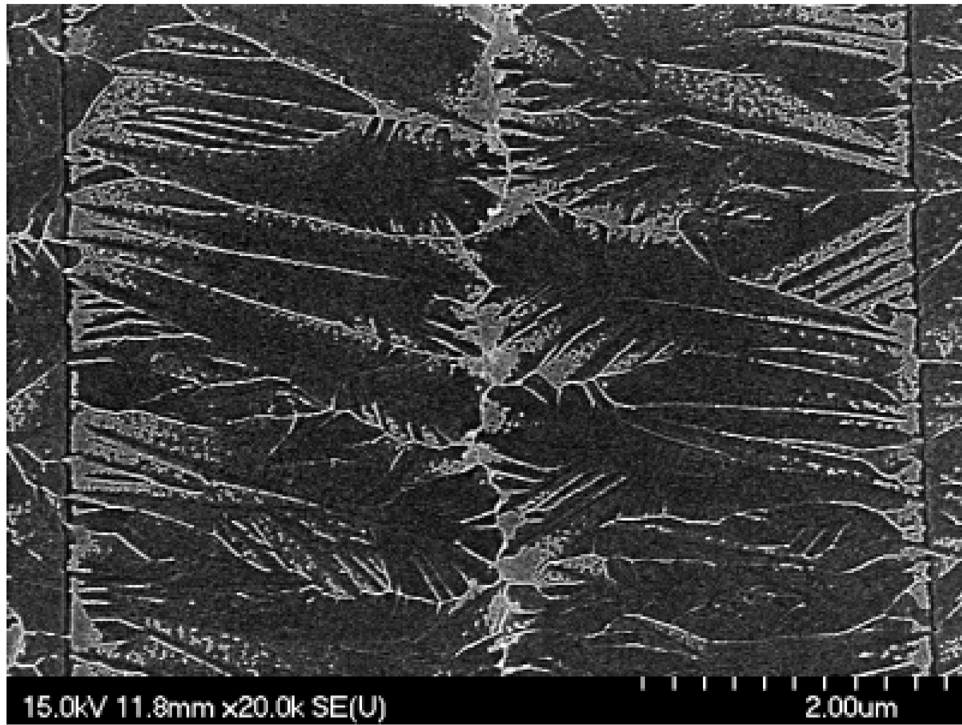

(c) Poly-$Si_{0.5}Ge_{0.5}$ 800mJ/cm^2

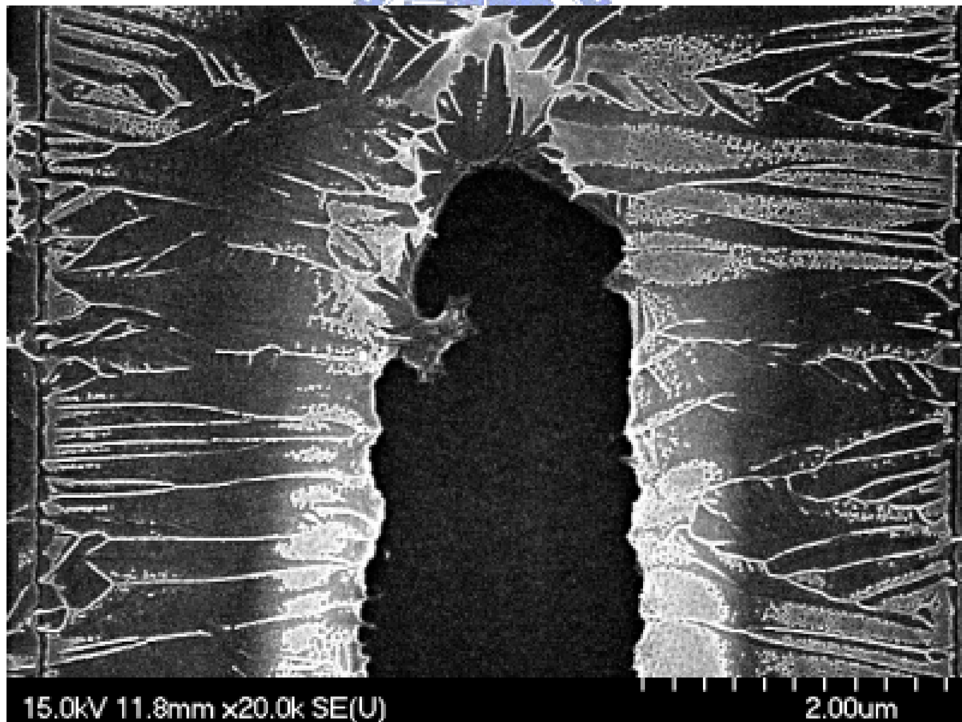

(d) Poly-$Si_{0.5}Ge_{0.5}$ 900mJ/cm^2

Figure 3-13α- $Si_{0.5}Ge_{0.5}$ Laser Crystallization after Secco etching

(I) - Side region

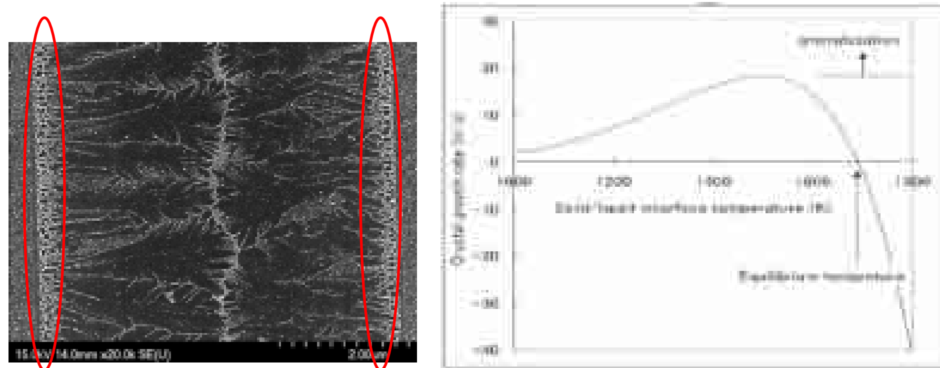

Super-cooling (Yeh and Matsumura 2000)

Figure 3-14 The proposed crystallization Mechanism for side region

(II) - Middle region

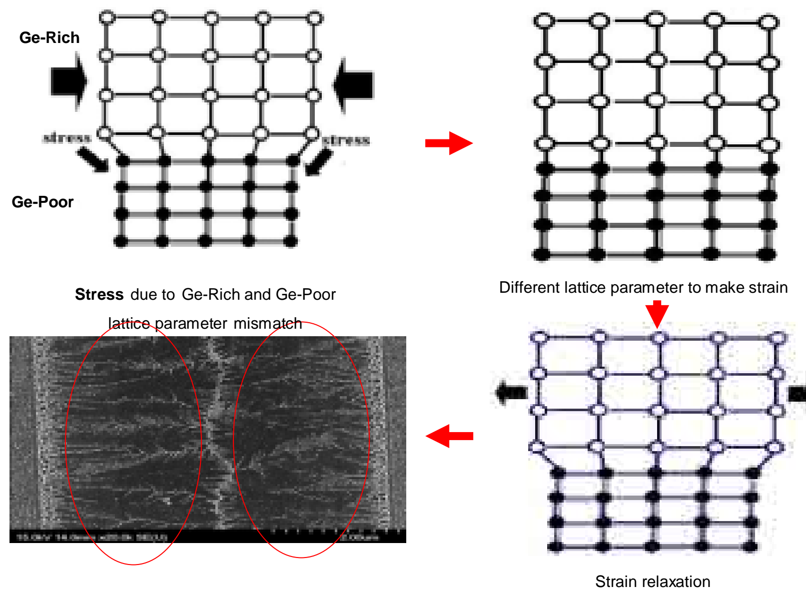

Figure 3-15 The proposed crystallization Mechanism for middle region

(III) - Grain Boundary

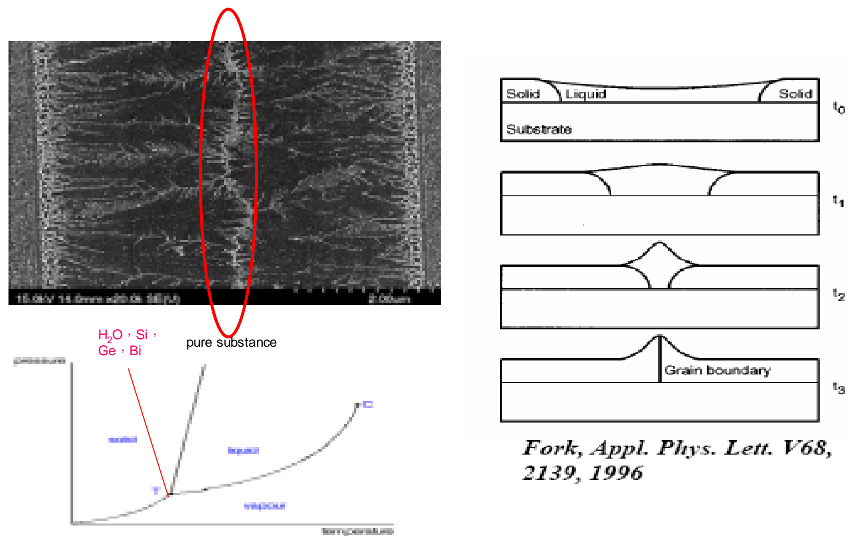

Figure 3-16 The proposed crystallization Mechanism for grain boundary

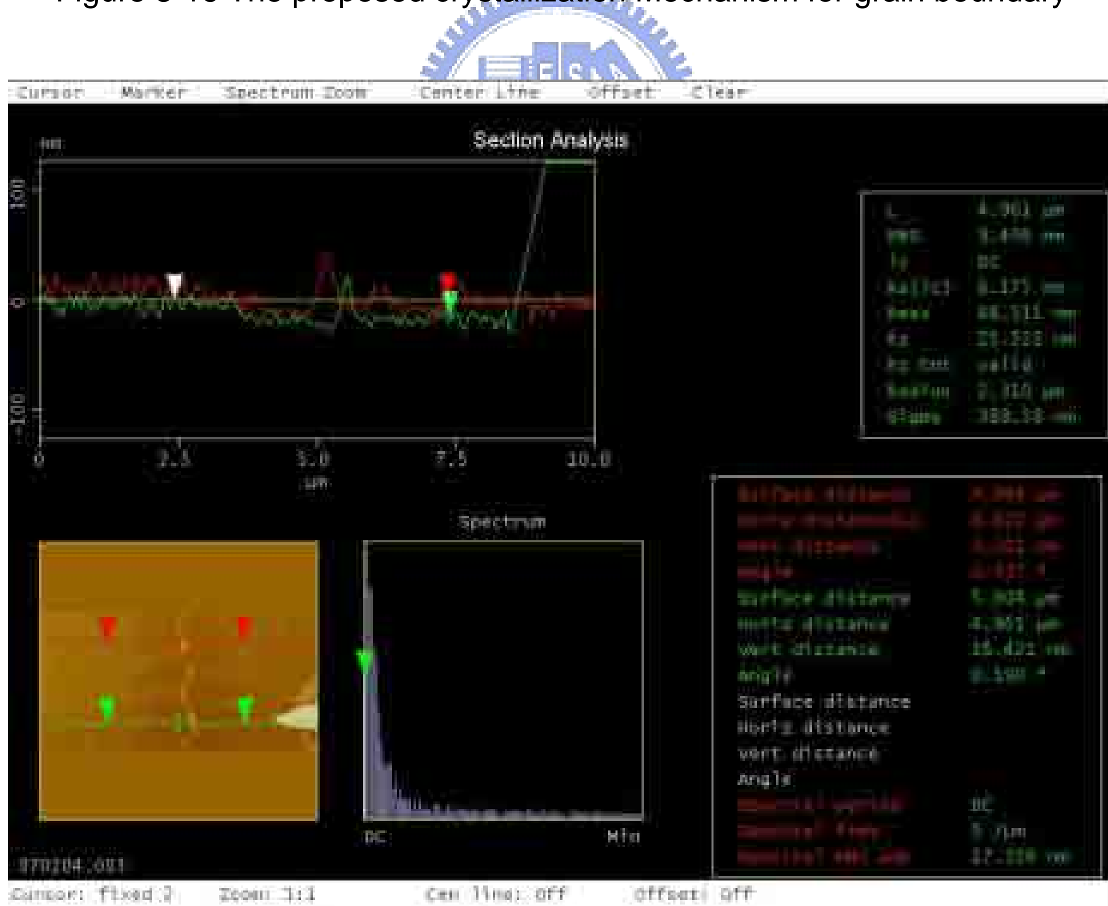

Figure 3-17 AFM micrographs of section analysis for poly-Si films irradiated by laser energy 800 mJ/cm^2

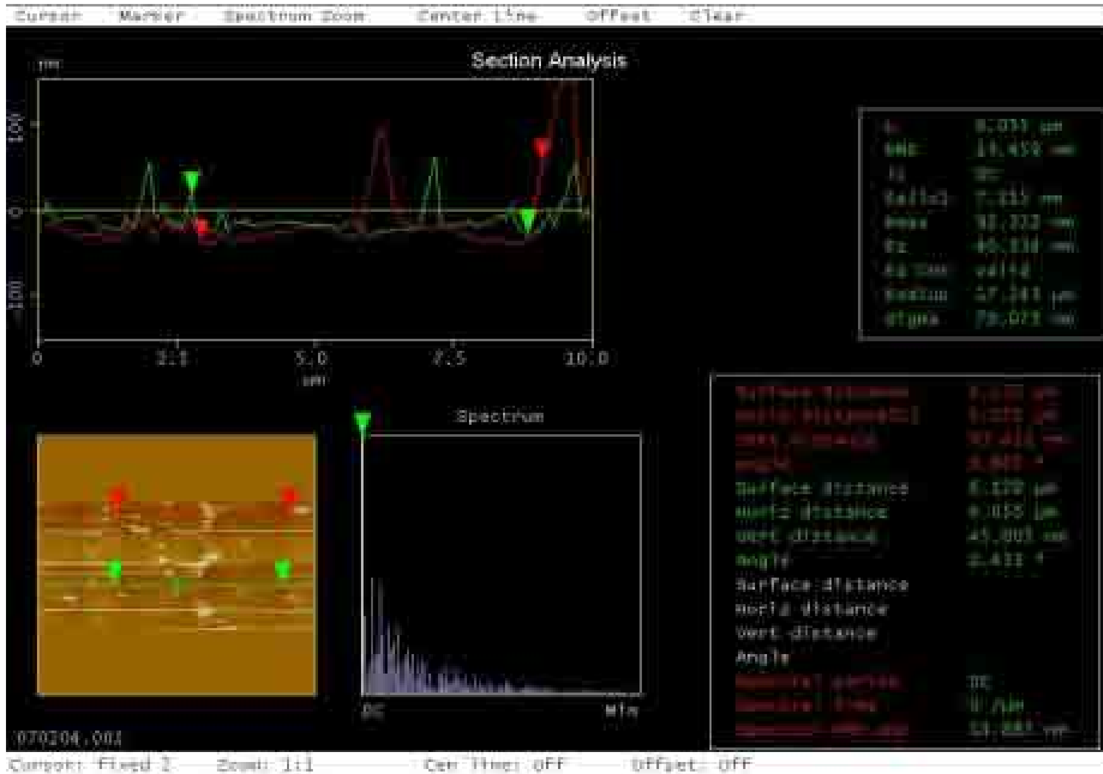

Figure 3-18 AFM micrographs of section analysis for poly-$Si_{0.66}Ge_{0.34}$ films irradiated by laser energy 800 mJ/cm^2

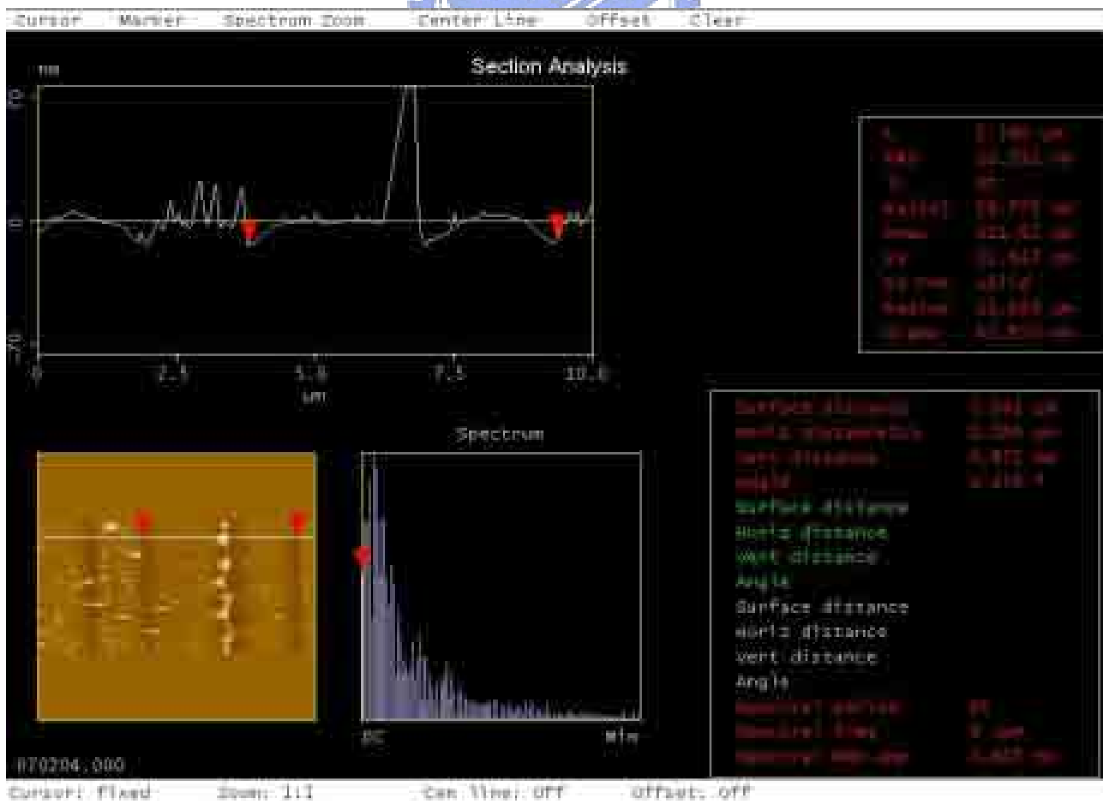

Figure 3-19 AFM micrographs of section analysis for poly-$Si_{0.5}Ge_{0.5}$ films irradiated by laser energy 800 mJ/cm^2

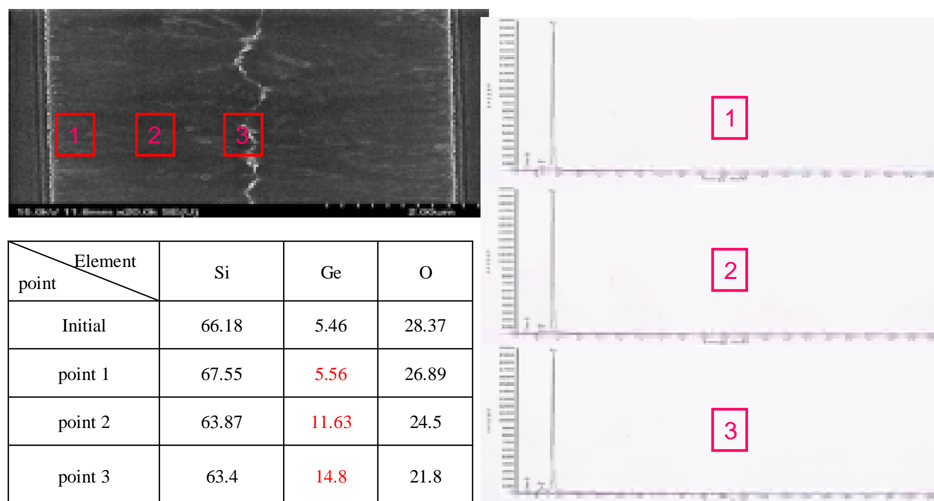

Element / point	Si	Ge	O
Initial	66.18	5.46	28.37
point 1	67.55	5.56	26.89
point 2	63.87	11.63	24.5
point 3	63.4	14.8	21.8

(a)

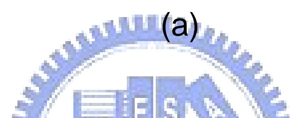

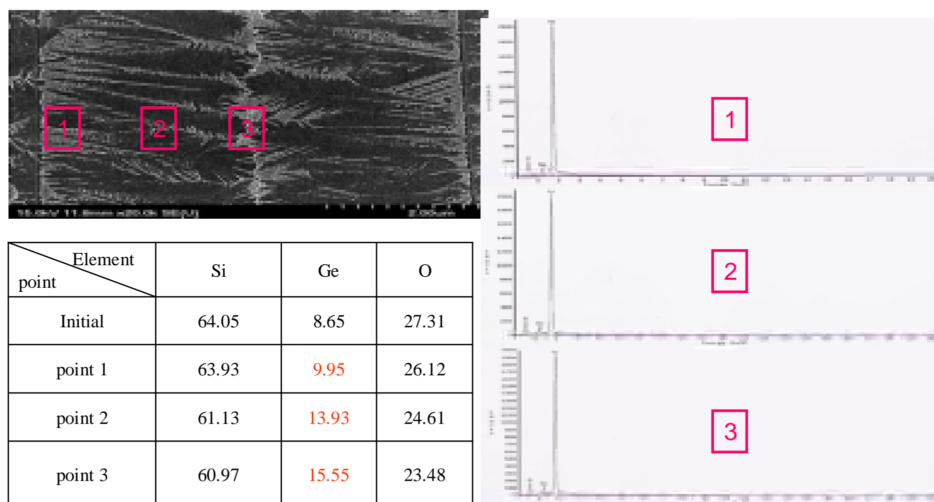

Element / point	Si	Ge	O
Initial	64.05	8.65	27.31
point 1	63.93	9.95	26.12
point 2	61.13	13.93	24.61
point 3	60.97	15.55	23.48

(b)

Figure 3-20 SEM micrographs and EDX analysis results of the (a) poly-$Si_{0.66}Ge_{0.34}$ thin film.(b) poly-$Si_{0.5}Ge_{0.5}$ thin film. E = 800mJ/cm^2

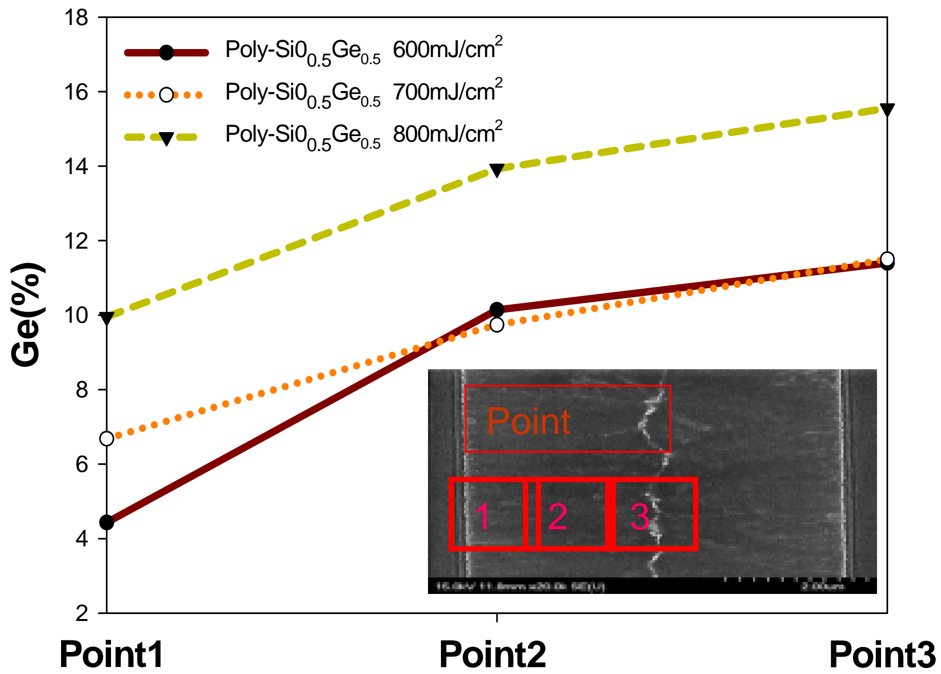

Figure 3-21 EDX analysis results of the poly-$Si_{0.66}Ge_{0.34}$ thin film with different laser energy

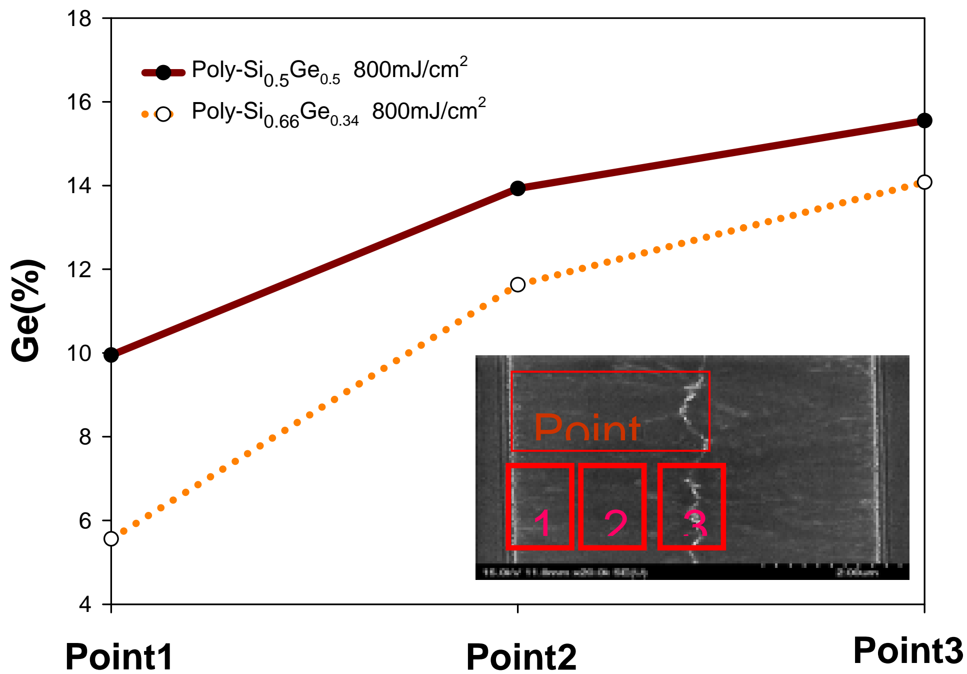

Figure 3-22 EDX analysis results of the poly-SiGe thin film with 800 mJ/cm^2

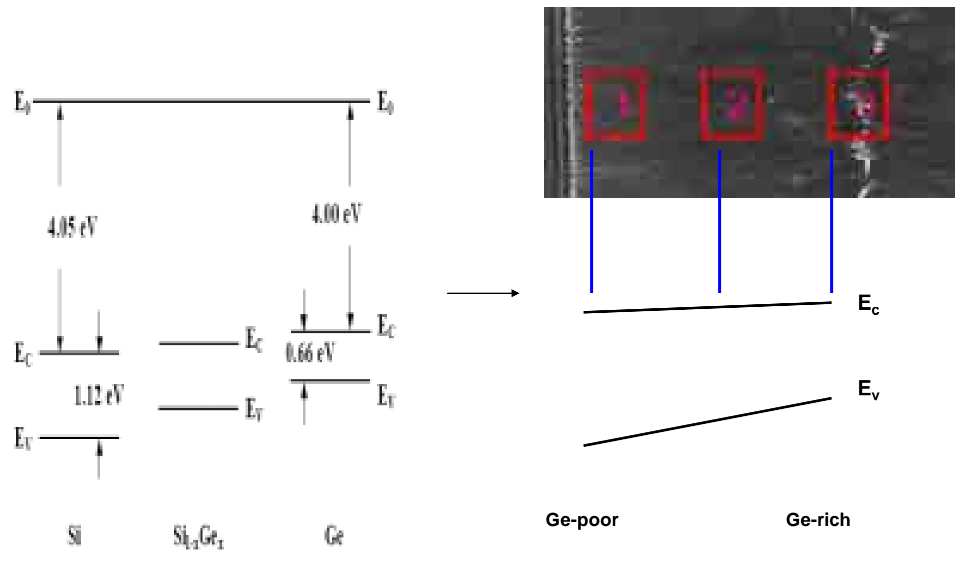

Figure 3-23 By grading the Ge content across the grain, the band gap will be different

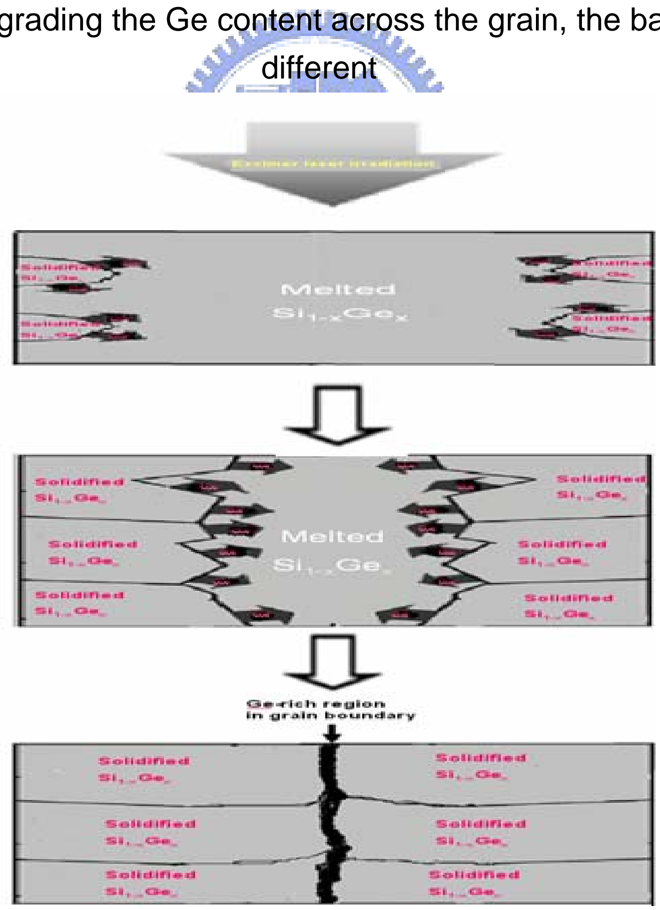

Figure 3-24 The proposed crystallization model for poly-Si1-xGex films crystallized by SLS-processing

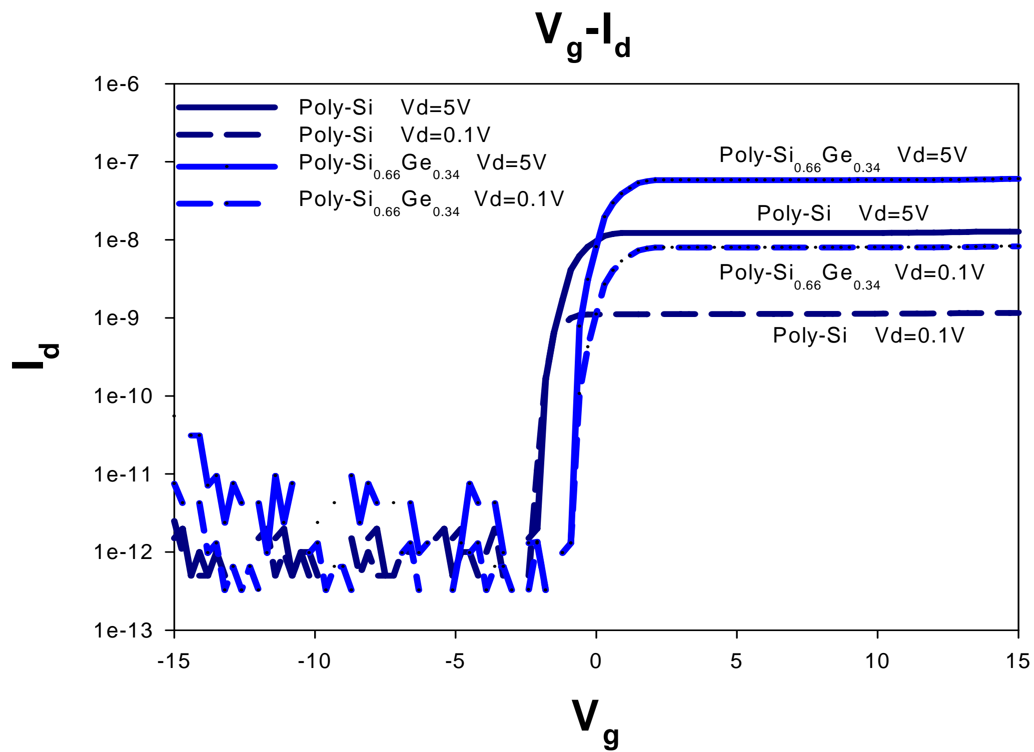

Figure 3-25 shows the I_d-V_g characteristic of poly-Si and poly-$Si_{0.66}Ge_{0.34}$ devices

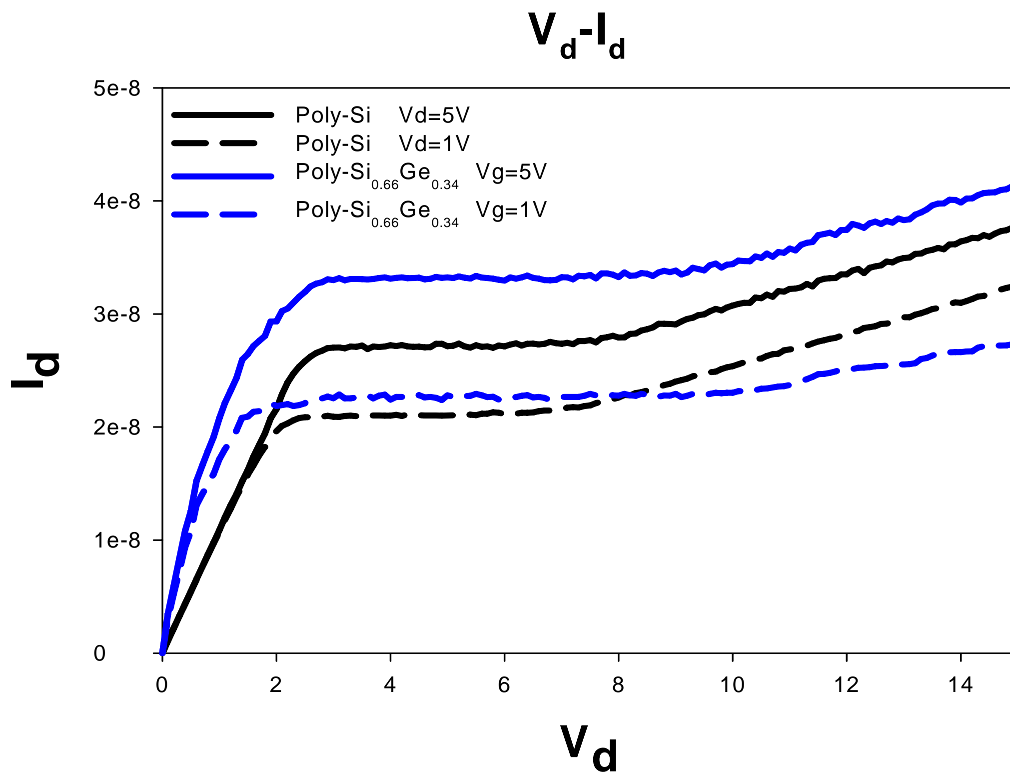

Figure 3-26 shows the I_d-V_d characteristic of poly-Si and poly-$Si_{0.66}Ge_{0.34}$ devices

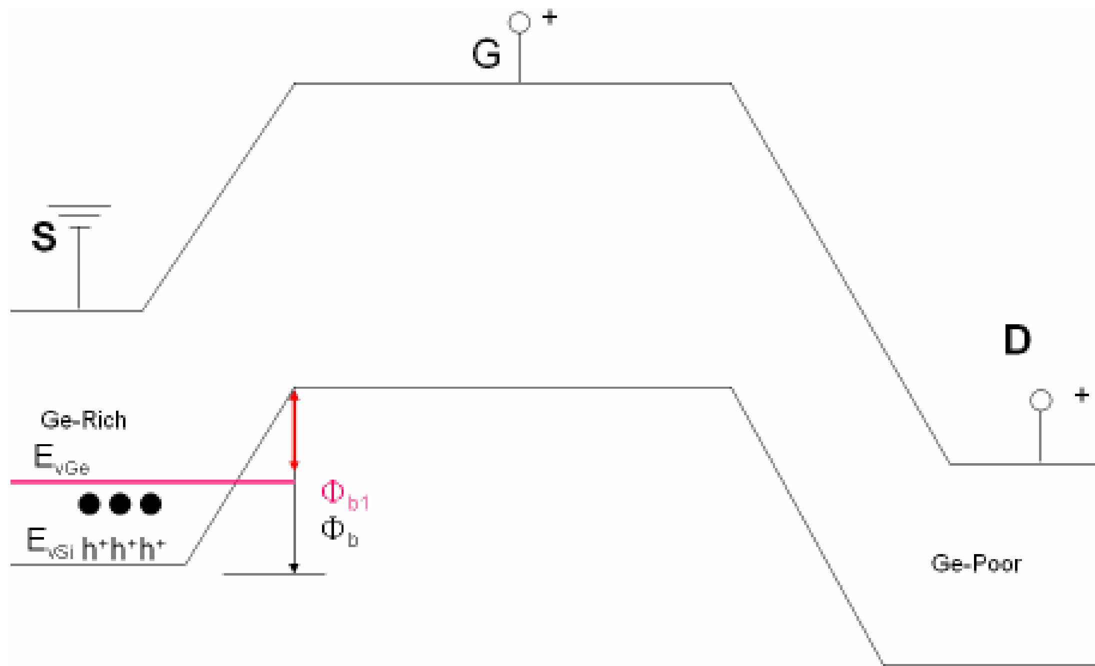

Figure 3-27 The proposed mechanism to improve floating body effect

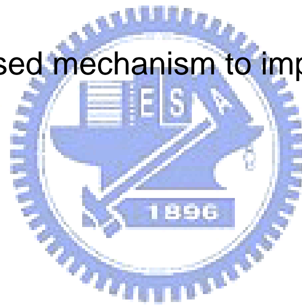

Chapter 4

Conclusion

In this thesis, we have shown that laser crystallization of $Si_{1-x}Ge_x$ thin film with x=0.34 and x=0.5 leads to a significant segregation into a Ge rich and poor areas. The deposition parameters and mechanisms of α-$Si_{1-x}Ge_x$ thin film by LPCVD have been studied in detail in chapter 3. To overcome the nucleation problem of the deposition of α-$Si_{1-x}Ge_x$ thin film on SiO2, a thin seed Si layer must be pre-deposited on SiO2. This manifests itself in a peak splitting in the Raman spectra. The position of the peaks in the Si–Si mode agree fairly well with segregation results obtained from EDX, indicating that the low frequency peak originates from the Ge rich area and the high frequency peak originates from the Ge poor area. The position of the peaks in the Ge–Ge and Si–Ge modes are shifted from their expected position according to the EDX results so that they always overestimate the Ge content. The strain almost relaxes after SLS-processing. The SEM micrographs of the SLS-processed poly- $Si_{1-x}Ge_x$ film after Secco etching show three growth mechanism and AFM to prove the grain boundary region.

By grading the Ge content across the transistor channel region, the band gap will be different. The different band gap can be use for channel region to improve Floating body effect.

References

Chapter 1

[1.1] Jun Hanari, "Development of a 10.4-in. UXGA display using low-temperature poly-Sitechnology," *Journal of the SID*, vol. 10, pp. 53-56, 2002.

[1.2] Yasuhisa Oana, "Current and future technology of low-temperature poly-Si TFT-LCDs,"*Journal of the SID*, vol. 9, pp. 169-172, 2001.

[1.3] Mutsumi Kimura, Ichio Yudasaka, Sadao Kanbe, Hidekazu Kobayashi, Hiroshi Kiguchi, Shun-ichi Seki, Satoru Miyashita, Tatsuya Shimoda, Tokuro Ozawa, Kiyofumi Kitawada, Takashi Nakazawa, Wakao Miyazawa, and Hiroyuki Ohshima, "Low-temperature polysilicon thin-film transistor driving with integrated driver for high-resolution light emitting polymer display," *IEEE Trans. Electron Devices*, vol. 46,pp. 2282-2288, 1999.

[1.4] Mark A. Crowder*, Member, IEEE*, A. Tolis Voutsas, Steven R. Droes, Masao Moriguchi, and Yasuhiro Mitani " *IEEE Trans. Electron Devices*, *VOL. 51, NO. 4, APRIL 2004*

[1.5] A. Hara, F. Takeuchi, and N. Sasaki, "Mobility enhancement limit of excimer-laser-crystallized polycrystalline silicon thin film transistor," *J. Appl. Phys.*,Vol. 91, pp. 708-714, 2002.

[1.6] T. Fujimura, A. Takami, A. Ishida, S. Kawamura, and T. Nishibe, "Reliability improvement of TFTs with thin gate insulator films by smoothing polycrystalline silicon surface roughness," in *AMLCD Tech. Dig.*, 2001, pp. 175-178.

[1.7] J. S. Im and R. S. Sposili, "Crystalline Si films for integrated activematrix

liquid-crystal displays," *MRS Bull.*, vol. XXI, no. 3, p. 39, 1996.

[1.8] H. J. Kim and J. S. Im, "New excimer-laser-crystallization method for producing large-grained and grain-boundary-location-controlled Si films for thin-film transistors," *Appl. Phys. Lett.*, vol. 68, no. 11, pp. 1513–1515, 1996.

[1.9] J. S. Im, M. A. Crowder, R. S. Sposili, J. P. Leonard, H. J. Kim, J. H. Yoon, V. V. Gupta, H. J. Song, and H. S. Cho, "Controlled super-lateral growth of Si films for microstructural manipulation and optimization," *Solid State Phys.* , vol. 166, pp. 603–617, 1998.

[1.10] R. S. Sposili and J. S. Im, "Sequential lateral solidification of thin silicon films on SiO ," *Appl. Phys. Lett.*, vol. 69, no. 19, pp. 2864–2866, 1996.

[1.11] J. S. Im, R. S. Sposili, and M. A. Crowder, "Single crystal Si films for thin-film transistor devices," *Appl. Phys. Lett.*, vol. 70, no. 25, pp. 3434–3436, 1997.

[1.12] S. D. Brotherton, M. A. Crowder, A. B. Limanov, and J. S. Im, "Characterization of poly-Si TFTs in directionally solidified SLS Si," in *Proc. Asia Display/IDW*, 2001, p. 387.

[1.13] T. J. King, K. C. Saraswat, and J. R. Pfiester, " PMOS transistors in LPCVD polycrystalline silicon-germanium films," *IEEE Electron Device Lett,*, vol. 12 p.p.584-586, 1991.

[1.14] J. B. Rem, M. C. V. de Leuw, J. Holleman, and J. F. Verweij, " Furnace and rapid thermal crystallization of amorphous GexSi1-x and Si for thin film transistors," *Thin Solid Films*, vol. 296, pp.152-156, 1997.

[1.15] Andrew J Tang, Julie A Tsai, and Rafael Reif, "A novel poly-silicon-capped poly-silicon-germanium thin film transistor," in

IEDM Tech. Dig., 1995, pp. 513-516.

[1.16] D. J. Gundlach, Y. Y. Lin, T. N. Jackson, S. F. Nelson, D. G. Schlom, "Pentacene organic thin-film transistors-molecular ordering and mobility," *IEEE Electron Device Lett.*, vol. 18, pp. 87-89, 1997.

[1.17] K. S. Choi and M. Matsumura, "Poly-Si/poly-SiC_x heterojunction thin-film transistors," *IEEE Trans. Electron Devices*, vol. 45, pp. 401-405, 1998.

[1.18] S. M. Choe, J. A. Ahn, and O. Y. Kim, "Fabrication of laser-annealed poly-TFT by forming a $Si_{1-x}Ge_x$ thermal barrier," *IEEE Electron Device Lett.*, vol. 22 , pp. 121-123, 2001.

[1.19] T. J. King and K. C. Saraswat, "Polycrystalline silicon-germanium thin-film transistors," *IEEE Trans. Electron Devices*, vol. 41, pp. 1581-1591, 1994.

[1.20] S. D. Brotherton, "Topical review: Polycrystalline silicon thin-film transistors," *Semicond. Sci. Technol.*, vol. 10, pp. 721–738, 1995.

[1.21] J. S. Im and R. S. Sposili, "Crystalline Si films for integrated activematrix liquid-crystal displays," *MRS Bull.*, vol. XXI, no. 3, p. 39, 1996.

[1.22] S.-W. Lee and S.-K. Joo, "Pd induced lateral crystallization of amorphous Si thin films," *Appl. Phys. Lett.*, vol. 66, p. 1671, 1995.

[1.23] T. J. King, K. C. Saraswat, " Polycrystalline silicon-germanium thin-film transistors,"*IEEE Trans. Electron Devices*, vol. 41, pp. 1581-1591, 1994.

Chapter 2

[2.1] J. Weber and M. I. Alonso, *Near-band-gap photoluminescence of Si-Ge alloys,* Phys. Rev. B (1989), **40**(8), p. 5683–5693.

[2.2] C. D. Thurmond, *The standard thermodynamic functions for the formation of electrons and holes in Ge, Si, GaAs, and GaP,* Journal of the Electrochemical Society (1975), **122**(8), p. 1133-1141.

[2.3] D. V. Lang, R. People, J. C. Bean, and A. M. Sergent, *Measurement of the band gap of GeSi/Si strained-layer heterostructures,* Applied Physics Letters (1985), **47**(12), p. 1333-1335.

[2.4] D. Dutartre, G. Brémond, A. Souifi, and T. Benyattou, *Excitonic photoluminescence from Si-capped strained SiGe layers,* Physical Review B (1991), **44**(20), p. 11525–11527.

[2.5] D. J. Robbins, L. T. Canham, S. J. Barnett, A. D. Pitt, and P. Calcott, *Near-bandgap photoluminescence from pseudomorphic SiGe single layers on silicon,* Journal of Applied Physics (1992), **71**, p. 1407-1414

[2.6] J. P. Dismukes, L. Ekstrom, and R. J. Paff, *Lattice Parameter and Density in Germanium-Silicon Alloys,* Journal of Physical Chemistry (1964), **68**(10), p. 3021- 3027.

[2.7] E. P. Kvam and R. Hull, *Surface orientation and stacking fault generation in strained epitaxial growth,* Journal of Applied Physics (1993), **73**(11), p. 7407-7411.

[2.8] J. W. Matthews and A. E. Blakeslee, *Defects in epitaxial multilayers,* Journal of Crystal Growth (1974), **27**, p. 118-125.

[2.9] B. W. Dodson and J. Y. Tsao, *Relaxation of strained-layer semiconductor structures via plastic flow,* Applied Physics Letters

(1987), **51**(17), p. 1325-1327.

[2.10] H. H. Radamson, A. Bentzen, C. Menon, and G. Landgren, *Observed Critical Thickness in Selectively and Non-Selectively Grown Si1-xGex Layers on Patterned Substrates,* Physica Scripta (2002), **T101**(1), p. 42-44.

[2.11] A. Nishida, K. Nakagawa, E. Murakami, and M. Miyao, *Elimination of misfit dislocations in $Si_{1-x}Ge_x$/Si heterostructures by limited-area molecular-beam epitaxial growth,* Journal of Applied Physics (1992), **71**(12), p. 5913-5917.

[2.12] D. B. Noble, J. L. Hoyt, C. A. King, J. F. Gibbons, T. I. Kamins, and M. P. Scott, *Reduction in misfit dislocation density by the selective growth of Si1–xGex/Si in small areas,* Applied Physics Letters (1990), **56**(1), p. 51-53.

[2.13] K. Kawaguchi, N. Usami, and Y. Shiraki, *Formation of relaxed SiGe films on Si by selective epitaxial growth,* Thin Solid Films (2000), **369**(1-2), p. 126-129.

[2.14] J.-M. Baribeau, *X-ray reflectometry study of interdiffusion in Si/Ge heterostructures,* Journal of Applied Physics (1993), **74**(6), p. 3805-3810.

[2.15] J.-M. Baribeau, R. Pascual, and S. Saimoto, *Interdiffusion and strain relaxation in (SimGen)p superlattices,* Applied Physics Letters (1990), **57**(15), p. 1502-1504.

[2.16] H. Brugger, E. Friess, G. Abstreiter, E. Kasper, and H. Kibbel, *Annealing effects in short period Si-Ge strained layer superlattices,* Semiconductor Science and Technology (1988), **3**(12), p. 1166-1170.

[2.17] J. S. Im, M. A. Crowder, R. S. Sposili, J. P. Leonard, H. J. Kim,J. H.

Yoon, V. V. Gupta, H. Jin Song, and H. S. Cho , " Controlled Super-Lateral Growth of Si Films for Microstructural Manipulation and Optimization," phys. stat. sol. (a) 166, 603 (1998)

[2.18] James S. Im and H. J. Kim, "On the super lateral growth phenomenon observed in excimer laser-induced crystallization of thin Si films," *Appl. Phys. Lett.*, vol. 64, pp.2303-2305, 1994.

[2.19] J. S. Im and R. S. Sposili, MRS Bull. 21, No. 3, 39 (1996).

[2.20] R. S. Sposili and J. S. Im, Appl. Phys. Lett. 69, 2864 (1996).

[2.21] R. S. Sposili, M. A. Crowder, and J. S. Im, Mater. Res. Soc. Symp. Proc. 452, 953 (1997).

[2.22] J. S. Im, R. S. Sposili, and M. A. Crowder, Appl. Phys. Lett. 70, 3434 (1997).

[2.23] B. Chalmers, Principles of Solidification, John Wiley & Sons, Inc., New York 1964.

[2.24] J. B. Rem, C. Salm, J. H. Klootwijk, M. H. H. Weusthof, J. Holleman, and J. F. Verweij, *Mater. Res. Soc. Symp. Proc.*, vol. 387, 1995, pp. 323.

Chapter 3

[3.1] M.I. Alonso, K. Winer, Phys. Rev. B 39 (1989) 10056

[3.2] M. Weizman[a,*], N.H. Nickel[a], I. Sieber[a], W. Bohne[a], J. Rfhrich[a], E. Strub[a], B. Yan[b]. "Phase segregation in laser crystallized polycrystalline SiGe thin films, "Thin Solid Films 487 (2005) 72– 76

[3.3] J. Groenen[a)] and R. Carles, S. Christiansen, M. Albrecht, W. Dorsch, and H. P. Strunk, H. Wawra and G. Wagner. "Phonons as probes in

self-organized SiGe islands", Appl. Phys. Lett., Vol. 71, No. 26, 29 December 1997

[3.4] Mark A. Crowder, *Member, IEEE*, A. Tolis Voutsas, Steven R. Droes, Masao Moriguchi, and Yasuhiro Mitani, "Sequential Lateral Solidification Processing for Polycrystalline Si TFTs", IEEE TRANSACTIONS ON ELECTRON DEVICES, VOL. 51, NO. 4, APRIL 2004